Published in final edited form as:

Nano Res. 2018 June ; 11(6): 3009–3030. doi:10.1007/s12274-018-2004-1.

Biomimetic Approaches Toward Smart Bio-hybrid Systems

Zhiqiang Luo[1], **Dara E. Weiss**[2], **Qingyun Liu**[1], and **Bozhi Tian**[2,3,4]

[1.]College of Life Science and Technology, Huazhong University of Science and Technology, Wuhan, Hubei 430074, PR China

[2.]Department of Chemistry, The University of Chicago, Chicago, IL 60637, USA

[3.]The James Franck Institute, The University of Chicago, Chicago, IL 60637, USA.

[4.]The Institute for Biophysical Dynamics, The University of Chicago, Chicago, IL 60637, USA

Abstract

Bio-integrated materials and devices can blur the interfaces between living and artificial systems. Microfluidics, bioelectronics and engineered nanostructures, with close interactions with biology at the cellular or tissue levels, have already yielded a spectrum of new applications. Many new designs emerge, including those of organ-on-a-chip systems, biodegradable implants, electroceutical devices, minimally invasive neuro-prosthetic tools, and soft robotics. In this review, we highlight a few recent advances on the fabrication and application of the smart bio-hybrid systems, with a particular emphasis on the three-dimensional (3D) bio-integrated devices that mimick the 3D feature of tissue scaffolds. Moreover, neurons integrated with engineered nanostructures for wireless neuromodulation and dynamic neural output will be briefly discussed. We will also go over the progress in the construction of cell-enabled soft robotics, where a tight coupling of the synthetic and biological parts is crucial for efficient functions. Finally, we summarize the approaches for enhancing bio-integration with biomimetic micro- and nanostructures.

Graphical Abstract

Address correspondence to Bozhi Tian, btian@uchicago.edu; Zhiqiang Luo, zhiqiangluo@hust.edu.cn.

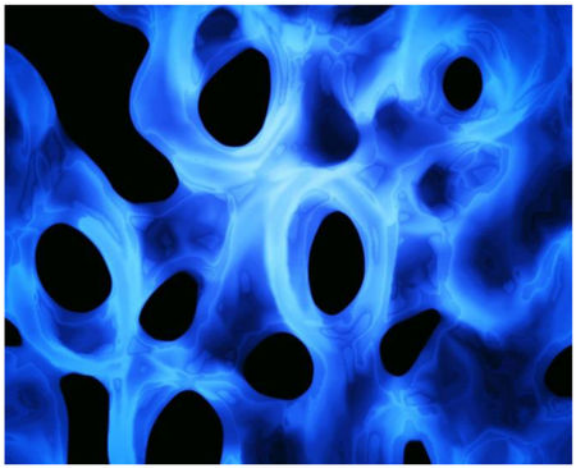

Building functional interfaces between living systems and artificial materials or devices is an emerging field. In this review, we highlight a few recent advances in the fabrication and application of seamlessly integrated bio-hybrid systems, with a particular emphasis on the three-dimensional (3D) constructs that recapitulate the features in naturally occurring systems.

Keywords

bio-integrated device; bio-hybrid system; biomimetics; nano-bio interface

1. Introduction

Bio-integrated devices with diagnostic and therapeutic capabilities play important roles in the healthcare industry [1–4]. Notable examples include cardiac pacemakers, deep brain stimulators, and artificial retinas. The performance of bio-integrated devices is determined by the efficacy of information and energy exchange at the interface between man-made devices and biological systems. Traditional implantable devices are prone to trigger a foreign body reaction, which is detrimental both for the human body and for the implanted devices [5, 6]. Additionally, the quality of the electrical signals passed across the biointerfaces can degrade over time due to the formation of scar tissues against the rigid device surfaces. To reduce the foreign body reaction and to enable a reliable signal transduction interface, tremendous amount of efforts have been put into developing mechanically less invasive bio-integrated devices using soft systems [7–10]. The soft bio-integrated devices are particularly advantageous in building a conformal interface with tissue surfaces possessing complex geometries and dynamics. However, the information and energy exchange between current soft bio-integrated devices and biological systems has been mostly limited in two-dimensional (2D) configurations. Since biological cells survive and function in the complex three-dimensional (3D) micro-environment, bio-hybrids that are engineered and integrated in 3D represents a more promising and advanced version of the bio-integrated systems. Lieber group at Harvard University is among those who explored the 3D and electrically “innervated” bio-hybrids [11–12]. These 3D bio-hybrids not only represent an innovative strategy to developing new generations of bio-integrated devices for

diagnostics and therapeutics [11–14], but also open up new opportunities for fundamental research, such as a smart organ-on-a-chip system for real time cell physiology studies [15, 16]. Moreover, the bio-hybrid platform also represents a new avenue for building “living” electronic or mechanic devices, such as engineered tissue-based soft robotics [17, 18].

In this article, we review the recent progress on the fabrication and application of a few classes of bio-hybrid systems. In section 2, we introduce the 3D constructs using folding/rolling methods and the 3D printing approach, with particular emphasis on achieving structures and functions that mimick the naturally occurring tissue scaffolds or extracellular matrices (ECM). We will also discuss the potential applications of 3D bio-hybrids for multifunctional organ-on-a-chip devices and biodegradable implants. The biological components covered in this section are largely synthetic or engineered. In section 3, we review recent advances of materials and devices that specifically used for neural interfaces, including examples of 3D macroporous nanoelectronics for brain probing and engineered ECM-like micro- and nanostructures for wireless neuromodulation. In section 4, we cover the progress in building soft robotics with engineered tissues. In particular, we discuss the potentials on mimicking the complex behaviors of cephalopods. In section 5, we highlight a few approaches for improving biointegration using biomimetic micro- and nanostructures, which exploit either unique morphologies or dynamic growth behaviors of inorganic materials. In the conclusion, we comment on future aspects in this area, and in particular approaches to promote tighter couplings between non-biological components with biological counterparts.

2. Biomimetic 3D Constructs for Engineered Tissues

Cells *in vivo* survive and function in a 3D micro-environment constructed and sustained by ECM. Substantial effort in tissue engineering has been made to construct 3D culture systems where biological, physical, and chemical cues are tailored to display similar features to those in natural ECM [19, 20]. The similar idea has been recently adopted for the development of bioelectronics open-framework for both *in vivo* and *in vitro* applications [11, 12]. In these cases, both the implementation of 3D electronic scaffolds and the incorporation of highly viable engineered tissues are critical for subsequent probing of cellular activities with high spatiotemporal resolutions [11, 12]. Seamless integration of 3D electronics throughout engineered tissues can lead to new fundamental and applied research activities, such as development of multifunctional organ-on-a-chip drug testing platforms and implantable bioelectronics that display minimum foreign body reactions.

2.1 Recent Advances in 3D Electronic Scaffolds

To construct engineered tissues within 3D electronic scaffolds, 3D interconnected device networks with tenths to hundreds of addressable nanoelectronic devices should be incorporated and eventually yield the following features: (a) macroporous open-framework device geometry to allow for interpenetration of cells and tissue clusters during development, (b) nano- or micron-scale structural features consistent with those in naturally occurring ECM, (c) 3D dispersion and individual addressability of the electronic devices, and (d) deformable mechanical properties similar to traditional biomaterials used for

engineered tissues. Lieber group demonstrated the first example of “cyborg tissues” through the integration of 3D nanoelectronic scaffolds and engineered tissues [21]. The 3D scaffolds were composed of interconnected nanoelectronic networks and conventional polymer scaffolds, such as Matrigel and poly(lactic-co-glycolic acid) (PLGA). The scaffolds exhibit macroporous forms, and a porosity exceeding 99%. Briefly, the devices were fabricated from 2D substrates with a standard lithographical method, where sacrificial layers were used to temporally support the planar device array. Consistent with those found in ECM, feature sizes ranging from tenths of micrometers (for interconnects, and their support or passivation layers) to tenths of nanometers (for silicon nanostructures typically used as electrical sensors) were typically considered for these constructs. To obtain 3D nanoelectronic scaffold, the 2D device layers were first released from the supporting substrates by etching the underlying sacrificial layers. Then, the partially freestanding device layers were constructed into 3D though either residual stress-induced self-organization or manual manipulation (Fig. 1). The final 3D nanoelectronic scaffolds were biocompatible and the silicon (Si) nanowire field effect transistor (FET) devices exhibited good electronic properties during cultures of multiple types of mammalian cells. In particular, using 3D nanoelectronic scaffolds consisting of 64 addressable nano-FET device arrays, Lieber group recently achieved real-time 3D mapping of electrophysiology activities in an engineered 3D cardiac tissue [22]. The 3D nanoelectronic scaffolds were fabricated by manual folding of nanoelectronic sheet into multiple layers with PLGA electrospun fibers, and with a 4×4 device array in each layer. With cardiomyocytes cultured inside the 3D nanoelectronic scaffold, extracellular cardiomyocyte action potentials (AP) were recorded with sub-millisecond temporal resolution. This real-time 3D recordings yielded quantitative maps for AP propagation and enabled in situ tracing of the evolving cardiac conduction pathways during the tissue development. Additionally, this platform was used to probe AP conduction characteristics in a transient arrhythmia disease model.

Integration of different devices, such as nanoscale FET (nanoFET), electrochemical sensors, strain and pressure sensors, photodetectors, light-emitting diodes, electrical stimulation electrode, etc., into single 3D macroporous nanoelectronic scaffolds would further broaden their capabilities for in vitro and in vivo applications. For example, Lieber group fabricated multifunctional 3D macroporous nanoelectronic scaffolds integrated with photodetectors, biochemical sensors, and strain sensors [23]. Since the conductivity of Si nanowire FETs changes upon illumination, they utilized the nanoFET as a photodetector for the determination of the device positions inside 3D nanoelectronic scaffolds. Simultaneous Si nanoFET photocurrent recording and confocal microscopy imaging were used to map the positions of the nanodevices throughout the 3D space of the tissue constructs with a resolution of ~14 nm [23]. In addition, the nanoFET can also serve as chemical and strain sensors for mapping time-dependent pH changes throughout a 3D gel sample and measuring strain field subject to uniaxial and bending forces, respectively. Recently, Dvir group expanded this concept into metal-based sensors and stimulators, and reported 3D electronic scaffolds with multiple functionalities of electrophysiology sensing, electrical stimulation, and controlled drug release triggered by electrical pulses [24]. They fabricated a 2D array of 32 gold (Au) electrodes on top of a flexible epoxy mesh, and then coated the device mesh with an electrospun nanofibre matrix made up of a polyester and gelatin. They then rolled or

folded the 2D composite scaffolds to provide a 3D structure for cardiac tissue growth. The Au electrode array recorded the cellular electrical activities, which enabled real time monitoring of cardiac tissue maturation and physiological activities. Additionally, Dvir group demonstrated that with on-demand provision of electrical stimulation, the seeded cells can be paced to contract synchronously, which is essential for cardiac tissue maturation. Finally, to achieve drug delivery, they fabricated large gold electrode pads that were coated with charged polymers. These polymers were used to electrostatically bind oppositely charged biomolecules, such as positively charged protein growth factors to enhance blood vessel growth, and negatively charged anti-inflammatory drugs. Electrical pulses were applied through the Au pads to change the polymer charges and triggered molecular release. The release of biochemical factors in a spatiotemporal manner complements the electrical stimulation, and offers a new control over cell growth and tissue maturation.

2.2 Expending Fabrication Approaches for 3D Bioelectronics

Aside from the folding and rolling of 2D nanoelectronic sheets into 3D scaffolds, several emerging techniques, including 3D printing, 3D lithography, strain-induce-self-assembly, and origami/kirigami of 2D “precursors”, represent new opportunities in fabrication of 3D bioelectronic scaffolds [25]. Although impressive advances have been achieved in fabrication of 3D biomaterials scaffolds using the 3D printing techniques [26, 27], their utilities in fabrication of 3D electronics only gained attention recently [28, 29]. Using multi-component 3D printing technique, Parker group integrated strain sensors, which were equipped with electrical readouts in cardiac organ-on-a-chip system for non-invasive and long-term recording of tissue contractile stresses inside cell incubator environment (Fig. 2) [30]. The strain sensors were printed using a thermoplastic polyurethane (TPU) ink filled with 25 wt% carbon black nanoparticles, while the electrical leads and contact pads were printed using a high-conductivity, silver particle-filled, polyamide ink. A polydimethylsiloxane (PDMS) layer with engineered micro-grooves was printed on the top surface to guide cardiomyocyte self-assembly into anisotropic laminar cardiac tissues, thus mimicking the structure of the native heart. The composite became free standing after the underlying dextran thin-film sacrificial layer was removed. Contraction of the anisotropic engineered cardiac tissue deflected a free standing cantilever construct, and therefore caused a resistance change in soft strain sensor embedded in the cantilever. Since the change in resistance is proportional to the contractile stress of the tissue, the recorded real-time signals were used for tracking the temporal development in tissue mechanics. This 3D printing approach enables new opportunities in developing smart organs-on-chips system to study cellular physiology and evaluate drug performance in vitro. This work also represents the first promising trial on full 3D printed devices composed of simple strain sensors; however, more work is needed to explore scalable 3D printing or 3D lithography techniques for bioelectronics with more functions and smaller feature sizes.

2.3 Degradation Considerations for Electronics Components

For *in vivo* implantation, the development of biodegradable devices may be considered for elimination of the device removal surgeries. Si is a degradable semiconductor material under physiological conditions. Recent studies suggest that biodegradation of Si can be caused by either oxidation of native dielectric SiO_2 layer into ortho-silicic acid $Si(OH)_4$ or a direct

hydrolysis of Si through the equilibrium of $Si+4H_2O \rightarrow Si(OH)_4+2H_2$ [31]. The biodegradation rate of Si depends on the crystalline form, doping level and environment parameters such as temperature and pH value [31]. The candidates of biodegradable metals, which can serve as source, drain and gate contacts for bioelectronics, include Mg, Zn, Fe, W and Mo [31–33]. For example, the Mg electrode can react with H_2O to form $Mg(OH)_2$ and the dielectric oxide layer MgO serves as a passive layer for electronic devices [31]. Using the above listed biodegradable electrical active materials, biodegradable passive dielectrics, as well as biodegradable substrates/encapsulation layers such as silk and PLGA film, Rogers group has extensively explored the fabrication of various resorbable or degradable devices including electrodes, strain/temperature/chemical sensors, complementary metal oxide semiconductor (CMOS) circuits, actuators, wireless communication devices, wireless power supply systems, and so on. Recently, they demonstrated *in vivo* transient spatiotemporal mapping of electrical activities and pressure recordings in a rat model using biodegradable electronics, where the constituent materials naturally undergoing biodegradation via hydrolysis and/or metabolic action [32, 33].

2.4 Strategies Towards Thicker Cellular Constructs

In order to implant large and thick electronics-containing bio-hybrids, future research would benefit from new device fabrication strategies. For example, a 3D microfluidic channel network with capability of nutrient/oxygen delivery and waste removal is of significant importance for large cellular construct where one would expect a high metabolic demand [34]. Recently, layer-by-layer assembly of lithographic modules was proposed by Radisic group to construct a 3D biodegradable microfluidic scaffold with a built-in vasculature (Fig. 3, a-d) [34]. A biodegradable and ultraviolet-polymerizable elastomer, poly(octamethylene maleate (anhydride) citrate) (POMaC), was used to fabricate a thin sheet with patterns using a photo-lithography method. Precise layer-by-layer stacking of the patterned POMaC sheet created a 3D branching network mimicking a vascular bed within a fully interconnected lattice matrix. The authors incorporated well-defined nanopores and micro-holes into the vascular walls, to allow efficient molecular exchange and cell migration. This approach can generate implantable and fully vascularized cardiac and hepatic tissue models (Fig. 3e,f). Moreover, the authors demonstrated direct in vivo surgical anastomosis of the cardiac tissue to the femoral vessels of rat hindlimbs (Fig. 3g). With these multiple level structures, the authors showed immediate host integration of the scaffolds which supported tissue survival for many weeks. However, the layer-by-layer assembled scaffolds did not recapitulate the fibrous nature of the cardiac ECM, which is essential for heart maturation. Through the combination of layer-by-layer assembly and deposition of electrospun fibers, Dvir group reported modular assembly of thick multifunctional 3D cardiac patches. To engineer anisotropic aligned cardiac tissues and create microchannels for forming blood vessels, electrospun fibrous layers were patterned by laser illumination to create microgrooves [35]. To mimick the variation in collagen alignment throughout the left ventricle wall, the authors assembled the laser-patterned electrospun fiber layers with a slight shift among adjacent layers. The authors also showed that electrospun fiber scaffolds can controllably release vascular endothelial growth factor (which promotes vascularization), or dexamethasone (an anti-inflammatory agent). In future work, the construction of 3D electronics-containing bio-hybrids could incorporate these two fabrication strategies.

3. Constructing Smart Bio-hybrids for Neuroprostheses

The performance of the neuroprosthesis ultimately rests on the electrode/neuron interfaces. Earlier generations of neural electrodes, such as multi-electrode arrays, generally employ materials with high conductivity, including metal (metal alloys and metal oxides) and highly doped semiconductors [36]. However, these commercially available electrodes are bulky and rigid, and they usually encounter inflammation, integration difficulties, long-term instability and power supply shortage problems [5, 6]. Decades of neuro-engineering research have aimed to blur the boundaries of the electrode/brain interface. Soft material electronics ameliorate many of the aforementioned drawbacks due to the similarity between their mechanical properties and those of biological tissues [7–10]. Recently, great developments in the geometry and mechanics of the designs of implantable 3D soft bioelectronics systems have been utilized to achieve an intimate interface for minimally invasive to non-invasive monitoring and manipulation [37–40].

3.1 3D Bio-hybrids for Brain Probing

Neuroprosthesis should be capable of physiological integration into the target neural tissues at cellular levels with high fidelity over the life span, and ideally, forming a symbiotic bio-hybrid. Recent efforts include attempting to realize a 3D, light-weight, flexible and implantable neuroprosthesis that could become part of the host body, thus enabling minimally-invasive probing [37, 38]. Lieber group made a significant step forward by developing a new class of intracortical probes using macroporous flexible mesh electronics [37]. The mesh electronics are completely released from substrate, whereby they allow for seamless and minimally invasive 3D interpenetration into the textured tissues by syringe injection (Fig. 4a). The electronics were driven by solution through a needle with an inner diameter less than 30 times the width of electronics and were subsequently delivered controllably into 3D structures (Fig. 4b). Notably, the same mesh electronics were injected into live rodent brains for long-term recording of brain activities. Most importantly, the authors showed that the injectable electronics yielded little chronic immunoreactivity in the brain of a mouse. As is shown in Fig. 4c, mesh electronics exhibited neurophilic characteristics and formed tight association with stained cells. A 3D confocal image from a hippocampus prepared five weeks post-injection (Fig. 4d) indicated limited astrocyte proliferation, and while healthy neurons were populated in the vicinity of mesh electronics, showing positive cellular interactions at the probe/tissue interface.

However, input/output (I/O) connections required in recording signals must be introduced after the injection of macroporous mesh electronics as they cannot pass through the injection needles. Lieber group in parallel developed an implantable 3D macroporous nanoelectronic neural probe with I/O directly connected to external electronics [38]. Fig. 4e shows optical photograph of the designed ideal implantable neural probe with a facile I/O connector to allow for multiplexed recording but not at the expense of macroporous and flexible properties. The magnified photograph shown in Fig. 4f (top) shows that the overall design of the electronics probe remains macroporous, with about 80% 2D open area, feature sizes to sub-10 μm scale and effective bending stiffness of <0.64×10–15 Nm^2. A positive transverse curvature is produced as the compressive strain elements are incorporated, yielding a

cylindrical global probe structure. Meanwhile, a negative curvature is generated with the integration of the local tensile strain element in the supporting arms of the sensor devices. The negative curvature manifests in the bending of the devices 100 μm away from the probe's cylindrical surface, therein facilitating interpenetration and intimate integration (Fig. 4f bottom). Thus, the bending allows the probe to expand easily in the brain without compromising the neuron. In order to study the macroporous nanoelectronic probes' in-vivo recording aptitude, the Lieber group then inserted the probes into rodent brains. Figure 4g displays the probe's ability to record multiplexed local field potentials in the somatosensory cortex, particularly nanowire FETs' (from a single probe) recording of strong multiplexed signals (amplitude of 3.4±0.3 mV). Duplicate multiplexed recording trials also produced comparable performances more than 10 times. Each trial produced greater than 80% active sensor yields. Furthermore, figures 4h-j exhibit the platinum electrode sensors' sharp millisecond spikes with a signal-to-noise ratio >7, denoting the sensor and the firing neuron were in close propinquity. Exploration of the probe-tissue histology shows the neural tissue's noninvasive chronic response to the ultra-flexible macroporous probe, attractive neuron-probe interactions, long-term stability and biocompatibility at the neural interface.

A recent study conducted by Xie group has reported a class of nanoelectronic thread (NET) probes with subcellular dimensions and ultrathin thickness [39]. The authors fabricated NET probes, with cross sections as small as 10μm × 1.5μm, in a seven-layer layout to host four electrodes on two opposite surfaces. They showed that the accommodating electrode array on a single ultra-small probe was able to record from brain regions with a large depth span, which provides new opportunities for minimally invasive 3D probing of the brain using high-density NET array. With *in vivo* imaging and histology studies, the authors revealed a scar-free interface, which shows great promise in enabling non-degrading neural probes. The structure of NET probes remains intact and impedance and recording performance remains stable for at least 4 months. The NETs meet several stringent requirements, including: small dimensions to ensure minimal perturbation to the host biological matrix, sufficient flexibility for complete compliance to tissue microenvironment and reduced probe-tissue interfacial force. Furthermore, minimal surgical damage allows for fast tissue recovery as well as mechanically and electrically robust chronical functionalities under the biological environment. Moreover, the ultra-flexible and ultra-small NETs show advantages in building a seamless dynamic interface for robust electrical performance. Over the period of several months, the neurons and NET probes locations are dynamic. Thus, the interface evolves according to the changing vasculature morphology and other microbiological environmental alterations.

3.2 Particle-based Bio-hybrids for Wireless Neuromodulation

Fully interconnected and electrode-based neural recording and stimulation are widely applied in clinical applications. Recently, several new concepts emerge and suggest intriguing alternatives [40]. For example, a recently reported skin-inspired organic digital mechanoreceptor is capable of directly inputting biomimetic electrical signals to the brain through remote stimulation [41]. The ring oscillator integrated digital mechanoreceptor mimics slow-adapting skin mechanoreceptors where output frequency responds sub-linearly to increasing force stimuli. In this case, mechanoreceptors detect and convert in situ pressure

signals from tactile sensors into optical signals that stimulate optogenetic somatosensory neurons in vitro. The basic process for optogenetics relies on genetic delivery and production of light-sensitive microbial ion channels and pumps, like channelrhodopsin, in the neural membranes [42]. As an alternative approach to optogenetics, new classes of non-genetic transducers, such as micro- and nanoparticles, have been used to convert the input stimuli into certain signals neurons can sense and respond to. The input signals, such as optical, magnetic and acoustic stimuli, are usually capable of noninvasive penetration through certain thicknesses of biological tissues to reach the particle-based transducers. In these approaches, the particles form hybrid interfaces with neurons, as we call bio-hybrids. These non-genetic and bio-hybrid enabled neuromodulations can be more generally applied and thus may be extensively adopted in the future [40, 43].

For example, biocompatible gold nanoparticles (AuNPs) capable of coupling with light through localized surface plasmon resonance (LSPR) have been explored for precise control of neural activities both *in vitro* and *in vivo* (Fig. 5 a and b) [44, 45]. When the AuNPs are bounded closely to neural plasma membrane, transient heating arises from the excitation of the LSPR mode in AuNPs, leading to a rapid increase in membrane temperature of neuronal cells. The local temperature rise can subsequently change the membrane capacitance and depolarize the cell membrane, which elicits action potentials [44]. This photo-thermal approach allows for neuromodulation at the subcellular resolution, although the optical power density levels still need to be improved. Aside from the triggering neuron activation with millisecond pulses of light, photo-thermal inhibition of neurons is also achievable using prolonged laser illumination [46]. Controllable activation and inhibition of neurons with light and non-biological materials would provide a promising therapeutic platform that operates wirelessly. Compared to AuNPs, semiconducting polymer nanobioconjugates (SPN) exhibit higher photo-thermal conversion efficiency [47]. The surfaces of SPN can be conjugated with anti-TRPV1 antibodies, yielding precise targeting of the TRPV1 ion channel, the most common heat-activated ion channel. In the exploration of biodegradable photothermal nanomaterials, Si-based semiconductor nanostructures have made progress [48]. As discussed in the previous section, Si can degrade under physiological condition. Tian group demonstrated recently a deformable form of Si mesostructures, featured with ordered nanowire-based framework, amorphous atomic structure, and submicrometer voids that are randomly distributed (Fig. 5 c-e) [48]. This heterogeneous and deformable form of Si shows more than two orders of magnitude smaller Young's modulus as compared to its single-crystalline Si. Being 'soft' in Si is desirable given its potential to reduce invasiveness when implanted. As shown in Fig. 5f, the amorphous Si mesostructures have fast photo-thermal dynamics. Upon laser illumination, the temperature of the Si mesostructures increased by a few degrees within milliseconds. This biodegradable form of Si is capable of subcellular modulation of the electrophysiology activities of neurons, and with single spike accuracy in certain range of optical excitation frequency. Since the heating is very brief in these cases, the side effects caused by heat to live cells may be less severe. However, the heat-induced cytotoxicity is still subjected to extensive future studies before clinical applications can be fully achieved.

Akin to photo-thermal stimulation, magnetic nanoparticles in an alternating magnetic-field can generate magneto-thermal effect to activate neurons (Fig. 5 g-i) [49–52]. Pralle group

demonstrated a remotely-controlled local heating of superparamagnetic manganese ferrite ($MnFe_2O_4$) nanoparticles, to convert radio-frequency magnetic signals into heating that eventually affected cell behaviors [49]. To avoid excess heat loss to the surrounding buffer fluid, magnetic nanoparticles, which were surface-modified for membrane-targeting, bonded to specific proteins on the plasma membrane of cells. This targeting of particles formed bio-hybrids and induced an increase in temperature that was highly localized to the immediate vicinity of the plasma membrane. The local temperature increase opened the TRPV1 channels and caused a Ca^{2+} influx in the cultured neurons, triggering their action potential without observable toxic effects. This approach was also efficient to trigger a behavioral response in *Caenorhabditis elegans*. It is interesting that tiny ferritin can also be used as a magneto-thermal transducer for remote control of cell activities [50]. The intracellular synthesis of magnetic nanoparticles was achieved in bioengineered cells that express ferritin. In this case, a ferritin fusion protein, composed of a ferritin light chain fused to a ferritin heavy chain with a flexible linker region, can help generate an iron core. Heating of the iron core by a radio-frequency magnetic field opened the TRPV1 channel to trigger calcium entry. Notably, the Anikeeva group extended the wireless magneto-thermal stimulation to *in-vivo* deep brain stimulation, where the authors used low-radio-frequency (100 kHz to 1 MHz) magnetic-field that is capable of penetrating the body without substantial attenuation [51, 52]. Magnetic nanoparticles with an optimized size of 20~30 nm were used to achieve high magneto-thermal performance and easy diffusion between the neurons in the brain. These nanoparticles were surface modified to enhance their stability in physiological fluids and targeted delivery to neurons. Initial magneto-thermal stimulation in deep brain region was demonstrated in ventral tegmental area (VTA) of mice [51]. The Anikeeva group showed the chronical utility of the magneto-thermal stimulation, as evidenced by the excitation of neurons in VTA by Fe_3O_4 magnetic nanoparticles one-month post-implantation. Most recently, it was demonstrated that magneto-thermal deep brain stimulation can evoke motor behavior in awake, free moving mice [52]. The Pralle group showed ambulation in the motor cortex as a result of the magneto-thermal stimulation. They also demonstrated rotation around the body axis as a result of deep-brain stimulation as well as freezing-of-gait from stimulation proximal to the ridge between the ventral and dorsal striatum [52].

Without the need for any surgical implantation and transgenesis, the particle-enabled neural-hybrid approach enables spatially targetable and temporarily precise modulation of neuron activities. Although promising, these smart bio-hybrids used for neuroprostheses still need extensive evaluations before reaching their clinical targets. Ultimately, to realize wireless neural interfaces in clinics, these new types of neuroprostheses would be coupled with other wearable devices for closed-loop applications. With a range of possibilities in device design and implementation, smart bio-hybrids may become the prevailing nervous disease therapy in the foreseeable future.

4. Engineered Tissue enabled Soft Robotics

Soft robotics is an emerging research field that aims to overcome the limitations of conventional rigid robotic systems through exploration of new soft materials and biomimetic designs [53]. Biological systems have evolved to display sophisticated mechanisms of

sensing, actuation, and adaptation when external stimuli are applied. Therefore, the integration of highly dynamic and adaptable cells or tissues with soft artificial systems represents a promising strategy to building intelligent soft robotics with the ability to process signals and adapt to external stimuli in real time [17, 18]. For example, using cardiomyocytes and muscles, which contract autonomously or upon electrical stimulation, bio-hybrid robotics have been designed to perform precisely controlled actuation and even net locomotion [54–57]. The integration of living cells into soft materials and devices would open up new avenues in the field of soft robotics for healthcare applications, including targeted and adaptive diagnostics and therapeutics *in vivo*.

4.1 Building a Soft Robot with Bio-hybrids

The Parker group reported a bio-hybrid robotic device in which synthetic cardiac tissues served as the actuator [54]. They coated flexible PDMS thin films with cardiomyocytes which were assembled with uniaxial alignment. Anisotropic contraction of cardiomyocytes can induce PDMS/cardiomyocyte bio-hybrids to perform motile functions such as gripping, pumping, walking, and swimming. In particular, when an electric stimulation was applied to this bio-hybrid, cardiomyocytes contracted synchronously and thus provided cohesive force to deform the PDMS thin films. Besides serving as a supporting substrate for cardiomyocytes, the PDMS elastomer also acted to restore the original shape if the cardiomyocytes came to a relaxation state. In this way, a propagating contractile wave was developed to actuate a bio-hybrid robot. Notably, with an electric field stimulus of a voltage amplitude of 10 V, pulse-width of 10 ms, and pacing frequency of 1 Hz, a triangular bio-hybrid robot swam with a maximum speed of 24 mm min^{-1}. Using a similar concept, the same group further developed a more sophisticated PDMS/cardiomyocytes bio-hybrid that resembled the jellyfish movement (Fig. 6) [55]. By coordinating the highly ordered myofibril organization with spatiotemporal contraction, the authors were able to emulate jellyfish muscle function. And specifically, they used quantitative structural designs that recapitulated the stroke kinematics and animal-fluid interactions, optimized PDMS geometry, and anisotropically engineered cardiac tissues to perform propulsion and feeding motions of jellyfish. To generate enough force, larger bundles of cellular assemblies may be needed for a more powerful bio-hybrid robot. As introduced in section 2, integration of a microfluidics network for oxygen and nutrient mass transport in bio-hybrid robots may meet this requirement.

A more sophisticated bio-hybrid system can be created through the integration of multiple cell types and composite materials, and 3D printing presents an ideal approach for this purpose. Using stereolithographic 3D printing of poly(ethylene glycol) diacrylate (PEGDA) hydrogel, Bashir group fabricated a 3D bio-robot skeleton composed of a flexible beam, mimicking an articulating joint, with two stiff pillars at each end. C2C12 skeletal muscle myoblasts and ECM proteins were added around the pillars and the pillars served as anchor points for tissue-engineered muscle strip [56, 57]. Upon electrical stimulation, cells in the muscle strip contracted and thus actuated the bio-hybrid robot. With finite-element simulations, they designed asymmetric 3D structures via a change in the length of one of the pillars to get asymmetric pillar displacements in response to muscle contraction. When electrically stimulated with 1 Hz frequency, the bio-hybrid robot achieved a maximum

velocity of 156 μm s^{-1}. Recently, the same group reported the integration of multiple cell types with this similar 3D platform [58]. Therein they explored the heterotypic co-cultures of skeletal muscles and motor neurons that were differentiated from mouse embryonic stem cells. The co-cultured tissues formed a neuromuscular junction, which efficiently induced muscle contraction upon chemical stimulation of motor neurons with neurotransmitter. With this modular cellular system, together with the 3D-printed hydrogel skeleton, the authors demonstrated a bio-hybrid robot that can be actuated by controllable release of glutamate, a major excitatory neurotransmitter in mammalian nervous system.

4.2 Responsive Bio-hybrids for Intelligent Soft Robot

The electric field stimuli used in the above studies were typically applied with Pt wire electrodes, which were placed far away from the cells inside a culture dish [54, 55]. This electrode configuration has limited the precise delivery of the electric field. To meet this challenge, researchers have integrated the cellular culture assembly with a high density microelectrode arrays to achieve localized stimulation with high spatial and temporal resolutions. This microelectrode arrays also enabled programmable control of the cellular actuation in both space and time domains. To this end, conductive soft materials such as PEDOT and carbon nanotubes (CNT) can be integrated into bio-hybrid robots to serve as underlying microelectrode arrays. For example, smart hydrogel electronics, which are composed of PEG hydrogel substrates, CNT forest electrode array, and CNT-methacrylol modified gelatin (GelMA) conductive hydrogel coating, was integrated with cardiac muscle tissue constructs [59]. In order to circumvent CNT delamination and improve the mechanical stability of the structure, CNT forest-based microelectrode arrays were layered between two thin hydrogel layers. The resulting surface was then used as a substrate to culture cardiomyocytes for induced maturation of cardiac muscle tissues. Microelectrode arrays were then implanted into the bio-hybrid construct. The resulting structure displayed exceptional mechanical and electrical efficacy. Thus, bio-hybrid robotics can be strictly controlled via external electrical fields emanating from the integrated CNT microelectrode arrays.

Compared to the electrical stimulation using electrodes in close proximity to or inside the bio-hybrid robot, wireless stimulation via an external signal is in high demand for untethered actuation and locomotion. Recently, both skeletal and cardiac muscle cells were genetically engineered for optogenetic light stimulation, and they were successfully used in the biohybrid soft robotic constructs [60, 61]. In this method, cells are genetically modified to express a light-activated cation channel that, when evoked with the proper wavelength of light, can initiate the cellular contraction. The advancements in optogenetics have made the optically-controlled bio-hybrid robotics possible. In a fantastic example, a light-responsive stingray analogue with the ability to swim adaptively was reported by Parker group (Fig. 7) [61]. They reverse-engineered the musculoskeletal structure of a stingray via a four-layered hybrid construct. A 3D PDMS body layer was casted with a titanium mold to form the synthetic bio-hybrid robot. Then, a metallic skeletal framework was developed using thermal evaporation of gold through a shadow mask. A spin-coated interstitial elastomer layer was then placed on the skeletal frame. Lastly, microscale patterning of fibronectin was used to produce a layer of undulating aligned cardiomyocytes, simulating muscle tissue with an

engineered density. These muscle tissues are used to imitate the sensory-somatic nervous system, triggering activation of fin muscles. Specifically, the individual muscles and sarcomeres of the engineered ray orient outwardly from the body and parallel to the gold skeletal rays. The optogenetic muscle layer contracts in a downward motion with optical stimulation, during which the asymmetrical stiff gold skeleton accumulates elastic energy and undergoes a successive relaxation phase. Such complex designs allow for spatial and temporal manipulation of muscle contractions, therein allowing for light stimuli based spatiotemporal control of fin movement, yielding movement analogous to that of the sting ray. However, the location of the light stimulus affects the direction of locomotion. For example, if the light stimulus is placed at the front of the stingray, the robot will swim forward.

Stimuli-responsive biological systems are not limited to the neuron and muscle cells, which elicit an electrophysiological response upon controlled external stimuli. Other interesting examples include leucophores and chromatophores, which enable cephalopods' ability to respond adaptively to dynamic environments (notebly camouflage) [62, 63].In cephalopods, the leucophores serve as diffuse reflectors that scatter light, the iridophores serve as dynamic Bragg stacks that reflect light, and the chromatophores serve as size-variable spectral filters that absorb/transmit light [62]. There are two control mechanisms for these stimuli-responsive cells: (a) chemical stimuli released from nerve fibers and (b) mechanical actuation from outward muscle fibers. Integrating the stimuli-responsive cells with soft microscale artificial systems would shift skin color-changing technology toward synthetic circuitry and away from nerve or muscle fibers. For example, to optimize color-changing beyond the capacity of the cephalopodan central nervous system, a bio-hybrid robot may utilize an integrated system comprised of 3D microfluidic networks of individually tunable channels and close-loop decision-making circuits containing a sophisticated and superior optical detector [64]. Other complex cephalopodan behaviors, such as shape morphing, would also be attractive objectives for the expansion of artificial circuit-controlled biomimetic machines. In order to mimic ambient structures, cephalopods develop papillae. Muscular hydrostats-integrated device system may replace the central nervous system and papillae for programmable morphing.

5. Enhanced Wet-adhesion for Integrated Bio-devices

The performance of bio-hybrids depends on the proper coupling of the devices to cells or tissues. Nature provides various inspirations for bio-adhesive surfaces, and mimicking biological wet attachment strategies is a booming research area [65–80]. Current approaches for wet bio-adhesion include interfacial chemical bonding with functional groups (e.g., NH_2, SH or COOH), and micro/nano-structuring of the device surfaces [65–80]. For improving the bioelectronics adhesion, chemical-based adhesives have some limitations, because the surface modifications may not be stable enough and they may also cause biocompatibility issues [65–67]. Modifying the device and substrate surfaces with biomimetic micro/nano-structures thus becomes more promising. Typical biomimetic micro/nano-structures showing good bio-integration mainly include (1) micro-/nano-pillar arrays coated with synthetic polymer that mimics the wet adhesive proteins [71–73], (2) mechanical interlock structures

[74–77], (3) octopus sucker cups [78–80]. Here we focus on the second and the last structures without any chemical coating.

5.1 Interlocking or Incorporation for Tissue Anchoring

Some natural biomaterials have anisotropic mesoscale features that can promote cellular or tissue-level interactions. If we inspect the structures of a bee's stinger, which can penetrate easily into human skin and then become deeply rooted, one will see anisotropic and graded structures that provide a novel mechanism for tissue anchorage. Such a mechanical interlocking effect may be explored in the future to design highly robust implants with enhanced bio-integration. With deposition-reconstruction cycles, Tian group developed a new lithography method, the atomic metal-enabled 3D chemical lithography, to yield Si mesostructures (i.e., Si spicules) that displayed bee's stinger-like morphology [74]. The 3D mesoscale lithography utilized the iterated deposition-diffusion-incorporation of atomic Au to form the etchant-resistant patterns for anisotropic alkaline-etching of Si. To quantitatively evaluate the potential for the enhanced biological integration, they mounted single Si structures onto atomic force microscopy (AFM) cantilever tips with a focused ion-beam system. They then recorded the force and work of the AFM cantilever tips in both the forward and reverse direction by approaching/retracting the spicules to/from a collagen hydrogel (Fig. 8 a-c). For the anisotropic Si spicules and un-etched nanowires with more uniform structures, the averages of the detachment force are 4.16 nN and 0.455 nN, and the averages of the detachment work are 20.0 fJ and 1.39 fJ, respectively, suggesting significantly enhanced integration with biological filaments due to the mesoscale mechanical interlocking effect. This material's anisotropy enhanced bio-integration may be broadly applied to medical implants or bioelectronics.

Another naturally occurring example of mechanically interlocked adhesive is the North American porcupine quills tip, which contains microscopic backward facing barbs that can hold tissue upon penetration [75]. Karp group made PDMS molds using North American porcupine quills, and then used a second step molding to form polyurethane (PU) replica [75]. The authors found that the average tissue adhesion force for barbed PU quills were 2.5 times higher than those of barbless PU quills and the work of removal for barbed PU quills were 30 times higher than those of barbless PU quills. The increase in the pull-out force was due to the mechanical interlocking of the barbs into the tissue. Inspired by the endoparasite Pomphorhynchus laevis, which swells its proboscis to attach to its host's intestinal wall, the same group later developed a novel water-responsive swelling method for large area fabrication of mechanical-interlocking microneedles with anisotropic mesoscale features [76]. The conical microneedles designed in a PDMS mold were comprised of two distinct strata. The inner stratum was designed from non-swellable polystyrene. Conversely, the upper stratum was made of a swellable poly(styrene)-block-poly(acrylic acid) (PS-b-PAA). The upper layer composed the tip of the microneedles (approximately 20% to 40% of the total height). The tip swelled with water when the needle was thrusted into the tissue, causing the needle to anchor into the tissue. The microneedles were then tested on the surface of intestinal tissue against a non-swellable polystyrene control. While the control microneedle adhesive had an adhesive strength of $0.48\pm0.18\ \mathrm{Ncm^{-2}}$, the swellable PS/PS-b-

PAA microneedles had an adhesive strength of 1.62±0.17 Ncm^{-2}, thus demonstrating improved, optimized mechanical properties.

Most recently, Tian group mimicked the placoid scale structures and explored dynamic growth of calcite matrices as focal adhesions for biological tissues (Fig. 8 d-g) [77]. The focal adhesion can be particularly helpful to bind soft and porous materials (e.g., biological tissues or hydrogels), as they are prone to irreversible damage when global adhesives are applied. They used the hard calcite and a soft matrix, such as PDMS, to mimick the scale and the epidermis/dermis components, respectively. The individual calcite heterostructure crystals exhibit asymmetrical dumbbell shapes, with one end embedded in soft device matrix (PDMS) and with the other end exposed for dynamic reactions. In this case, the exposed ends can gradually incorporate collagen fibrils of the skin tissues under the calcite growth condition, thus achieving bio-integration. It was found that upon collagen incorporation, the representative detachment force and work were 1 ~ 2 orders of magnitude higher than that of the collagen-free calcites samples. The tests on flexible calcite heterostructure matrices attached to rat skin tissues showed that the adhesion strength and the work of adhesion were both within the ranges of those recorded from other underwater adhesives.

5.2 Suction Cup for Wet Adhesion

A fascinating example of wet adhesion is the octopus' suckers. A volume differential in the sucker cavity is created by a pressure differential controlled by muscular action and motion, allowing for the sucker to adhere to virtually any extracorporeal surface [78, 79]. Recently, a nanosucker array was designed from a spin-coated 2D colloidal silica array template. The nanosucker array was made of PDMS and contained a hemispheric-like cavity [78]. The nanosuckers then underwent deformation in order to create a negative pressure differential and induce adhesion. Interestingly, the nanosuckers exhibited impressive adhesive capabilities on microrough and flat, wet and dry surfaces alike. In order to mimic a switchable cavity-pressure-induced adhesion, Lee et al. proposed the fabrication of suction adhesion pad using shape-programmable soft matter [79]. Shape-programmable soft matter materials may be volumetrically manipulated using external stimuli, making them optimal for a pressure differential based adhesion. Using a micro-cavity array patterned PDMS film and a thermoresponsive poly(N-isopropylacrylamide) (pNIPAM) hydrogel layer, the nanosuckers were fabricated into an adhesive material, forming the suction pad. Volumetric control of the nanosucker cavity can be further achieved through thermal manipulation. The pNIPAM hydrogel layer mechanically responds to changes in temperature, undergoing a contractile change at 32℃. Thus, the hydrogel layer may be considered an actuator as it contracts and relaxes, particularly with thermal stimulus. As the layer contracts and relaxes, the volume of the cavity decreases and increases, inversely affecting the pressure. Once the pressure differential is created, adhesion occurs. Therefore, by controlling the thermal stimulus' temperature, the adhesion of the pad may also be controlled.

However, the controllable pressure differential is not the only factor in the pad's adhesion. The subtle morphology of the nanosucker greatly affects its ability to adhere to foreign surfaces. In the case of the octopus, the suckers are dome-shaped, purportedly increasing their wet adhesive strength [80]. Baik et al. developed a tandem partial-filling and reverse-

molding technique to replicate the domed morphology of the octopus' suckers and their adhesive strength (figure 8 h-i) [80]. First, they created the polyurethaneacrylate-based polymer (s-PUA) master by partially filling its liquid precursor into the micro-scale holes of a silicon mould. The partial-filling technique helps create polymeric cylinder arrays with a spherical void in each cylinder, and it is based on the force balance among phase interfaces [80]. Subsequently, they replicated this polymeric architecture reversely to produce 'dome-in-a-cup' structures. Baik et al. found that not only could the synthetic suckers produced from this novel, tandem technique adhere to wet surfaces, they were able to do so better than synthetic suckers with simple holes. However, increased adhesive strength with their novel suckers was only possible in wet environments. In a dry environment, the domed suckers performed similarly to the non-domed, simple-holed synthetic suckers. Wet adhesion is increased in domed suckers due to capillary action resulting from a mixed interface between the dome and the substrate. Evidence supporting this rationalization for the difference in adhesive capacities of the domed suckers was provided by the authors who modeled and performed formulaic analysis of capillary-assisted suction in wet conditions.

6. Outlook

In conclusion, the integration of cellular components with non-biological materials and devices can lead to various new platforms and applications, such as a smart organ-on-a-chip system, a biodegradable implant, an electroceutical device, a minimally invasive neuro-prosthesis, and a soft bio-hybrid robotic construct. From a material perspective, the bio-hybrid system needs further development in the following directions: (1) development of scalable 3D printing or lithography approaches to fabricate bio-hybrid device arrays with smaller feature sizes and higher integration capacity. (2) better integration of biomimetic micro/nano-structures into bioelectronics or other emerging devices to achieve enhanced bio-integration, as a tight and reliable interface is central to any type of signal transductions; (3) realization of close-looped bio-hybrids through integration of multiple advanced device components, such as a wireless transductor, CMOS or even neuromorphic circuits, and built-in regulators. It can be envisioned that a 'cyborg' brain where new interfaces are established between neurons and multifunctional bio-hybrids that display synaptic-like plasticity [81]. Current large-scale memrisistor networks have reached a sufficient level of sophistication for the emulation of many of the neuronal behaviors [82]; further research is required to make the memrisistor network smaller, softer and biocompatible [83]. Finally, the smart bio-hybrids can lead to the creation of new cellular materials that have the potential to open up completely new areas of application, such as in hybrid information processing systems.

Acknowledgements

Zhiqiang Luo acknowledges support from National Natural Science Foundation of China (NSFC, No.81771974). Bozhi Tian acknowledges a primary support from the University of Chicago Materials Research Science and Engineering Center, which is funded by National Science Foundation under award number DMR-1420709. Bozhi Tian also acknowledges support from the National Institutes of Health (NIH 1DP2NS101488).

References

[1]. Hyam JA; Kringelbach ML; Silburn PA; Aziz TZ; Green AL The autonomic effects of deep brain stimulation--a therapeutic opportunity. Nat Rev Neurol 2012, 8, 391–400. [PubMed: 22688783]

[2]. Jackson A; Zimmermann JB Neural interfaces for the brain and spinal cord--restoring motor function. Nat Rev Neurol 2012, 8, 690–699. [PubMed: 23147846]

[3]. Birmingham K; Gradinaru V; Anikeeva P; Grill WM; Pikov V; McLaughlin B; Pasricha P; Weber D; Ludwig K; Famm K Bioelectronic medicines: a research roadmap. Nat Rev Drug Discov 2014, 13, 399–400. [PubMed: 24875080]

[4]. Fox D The shock tactics set to shake up immunology. Nature 2017, 545, 20–22. [PubMed: 28470211]

[5]. Kozai TD; Jaquins-Gerstl AS; Vazquez AL; Michael AC; Cui XT Brain tissue responses to neural implants impact signal sensitivity and intervention strategies. ACS Chem Neurosci 2015, 6, 48–67. [PubMed: 25546652]

[6]. Gunasekera B; Saxena T; Bellamkonda R; Karumbaiah L Intracortical recording interfaces: current challenges to chronic recording function. ACS Chem Neurosci 2015, 6, 68–83. [PubMed: 25587704]

[7]. Lacour SP; Courtine G; Guck J Materials and technologies for soft implantable neuroprostheses. Nature Reviews Materials 2016, 1, 16063.

[8]. Jeong JW; Shin G; Park SI; Yu KJ; Xu L; Rogers JA Soft materials in neuroengineering for hard problems in neuroscience. Neuron 2015, 86, 175–186. [PubMed: 25856493]

[9]. Choi S; Lee H; Ghaffari R; Hyeon T; Kim DH Recent Advances in Flexible and Stretchable Bio-Electronic Devices Integrated with Nanomaterials. Adv Mater 2016, 28, 4203–4218. [PubMed: 26779680]

[10]. Green R; Abidian MR Conducting Polymers for Neural Prosthetic and Neural Interface Applications. Adv Mater 2015, 27, 7620–7637. [PubMed: 26414302]

[11]. Tian B; Lieber CM Synthetic nanoelectronic probes for biological cells and tissues. Annu Rev Anal Chem (Palo Alto Calif) 2013, 6, 31–51. [PubMed: 23451719]

[12]. Duan X; Fu TM; Liu J; Lieber CM Nanoelectronics-biology frontier: From nanoscopic probes for action potential recording in live cells to three-dimensional cyborg tissues. Nano Today 2013, 8, 351–373. [PubMed: 24073014]

[13]. Zimmerman J; Parameswaran R; Tian B Nanoscale Semiconductor Devices as New Biomaterials. Biomater Sci 2014, 2, 619–626. [PubMed: 27213041]

[14]. Cohen-Karni T; Langer R; Kohane DS The smartest materials: the future of nanoelectronics in medicine. ACS Nano 2012, 6, 6541–6545. [PubMed: 22850578]

[15]. Esch EW; Bahinski A; Huh D Organs-on-chips at the frontiers of drug discovery. Nat Rev Drug Discov 2015, 14, 248–260. [PubMed: 25792263]

[16]. Guan A; Hamilton P; Wang Y; Gorbet M; Li Z; Phillips KS Medical devices on chips. Nature Biomedical Engineering 2017, 1, 0045.

[17]. Feinberg AW Biological Soft Robotics. Annu Rev Biomed Eng 2015, 17, 243–265. [PubMed: 26643022]

[18]. Patino T; Mestre R; Sanchez S Miniaturized soft bio-hybrid robotics: a step forward into healthcare applications. Lab Chip 2016, 16, 3626–3630. [PubMed: 27550016]

[19]. Dvir T; Timko BP; Kohane DS; Langer R Nanotechnological strategies for engineering complex tissues. Nat Nanotechnol 2011, 6, 13–22. [PubMed: 21151110]

[20]. Bajaj P; Schweller RM; Khademhosseini A; West JL; Bashir R 3D biofabrication strategies for tissue engineering and regenerative medicine. Annu Rev Biomed Eng 2014, 16, 247–276. [PubMed: 24905875]

[21]. Tian B; Liu J; Dvir T; Jin L; Tsui JH; Qing Q; Suo Z; Langer R; Kohane DS; Lieber CM Macroporous nanowire nanoelectronic scaffolds for synthetic tissues. Nat Mater 2012, 11, 986–994. [PubMed: 22922448]

[22]. Dai X; Zhou W; Gao T; Liu J; Lieber CM Three-dimensional mapping and regulation of action potential propagation in nanoelectronics-innervated tissues. Nat Nanotechnol 2016, 11, 776–782. [PubMed: 27347837]

[23]. Liu J; Xie C; Dai X; Jin L; Zhou W; Lieber CM Multifunctional three-dimensional macroporous nanoelectronic networks for smart materials. Proc Natl Acad Sci U S A 2013, 110, 6694–6699. [PubMed: 23569270]

[24]. Feiner R; Engel L; Fleischer S; Malki M; Gal I; Shapira A; Shacham-Diamand Y; Dvir T Engineered hybrid cardiac patches with multifunctional electronics for online monitoring and regulation of tissue function. Nat Mater 2016, 15, 679–685. [PubMed: 26974408]

[25]. Zhang Y; Zhang F; Yan Z; Ma Q; Li X; Huang Y; Rogers JA Printing, folding and assembly methods for forming 3D mesostructures in advanced materials. Nature Reviews Materials 2017, 2, 17019.

[26]. Murphy SV; Atala A 3D bioprinting of tissues and organs. Nat Biotechnol 2014, 32, 773–785. [PubMed: 25093879]

[27]. Do AV; Khorsand B; Geary SM; Salem AK 3D Printing of Scaffolds for Tissue Regeneration Applications. Adv Healthc Mater 2015, 4, 1742–1762. [PubMed: 26097108]

[28]. Kong YL; Gupta MK; Johnson BN; McAlpine MC 3D Printed Bionic Nanodevices. Nano Today 2016, 11, 330–350. [PubMed: 27617026]

[29]. Shin SR; Farzad R; Tamayol A; Manoharan V; Mostafalu P; Zhang YS; Akbari M; Jung SM; Kim D; Comotto M; Annabi N; Al-Hazmi FE; Dokmeci MR; Khademhosseini A A Bioactive Carbon Nanotube-Based Ink for Printing 2D and 3D Flexible Electronics. Adv Mater 2016, 28, 3280–3289. [PubMed: 26915715]

[30]. Lind JU; Busbee TA; Valentine AD; Pasqualini FS; Yuan H; Yadid M; Park SJ; Kotikian A; Nesmith AP; Campbell PH; Vlassak JJ; Lewis JA; Parker KK Instrumented cardiac microphysiological devices via multimaterial three-dimensional printing. Nat Mater 2017, 16, 303–308. [PubMed: 27775708]

[31]. Hwang SW; Tao H; Kim DH; Cheng H; Song JK; Rill E; Brenckle MA; Panilaitis B; Won SM; Kim YS; Song YM; Yu KJ; Ameen A; Li R; Su Y; Yang M; Kaplan DL; Zakin MR; Slepian MJ; Huang Y; Omenetto FG; Rogers JA A physically transient form of silicon electronics. Science 2012, 337, 1640–1644. [PubMed: 23019646]

[32]. Kang SK; Murphy RK; Hwang SW; Lee SM; Harburg DV; Krueger NA; Shin J; Gamble P; Cheng H; Yu S; Liu Z; McCall JG; Stephen M; Ying H; Kim J; Park G; Webb RC; Lee CH; Chung S; Wie DS; Gujar AD; Vemulapalli B; Kim AH; Lee KM; Cheng J; Huang Y; Lee SH; Braun PV; Ray WZ; Rogers JA Bioresorbable silicon electronic sensors for the brain. Nature 2016, 530, 71–76. [PubMed: 26779949]

[33]. Yu KJ; Kuzum D; Hwang SW; Kim BH; Juul H; Kim NH; Won SM; Chiang K; Trumpis M; Richardson AG; Cheng H; Fang H; Thomson M; Bink H; Talos D; Seo KJ; Lee HN; Kang SK; Kim JH; Lee JY; Huang Y; Jensen FE; Dichter MA; Lucas TH; Viventi J; Litt B; Rogers JA Bioresorbable silicon electronics for transient spatiotemporal mapping of electrical activity from the cerebral cortex. Nat Mater 2016, 15, 782–791. [PubMed: 27088236]

[34]. Zhang B; Montgomery M; Chamberlain MD; Ogawa S; Korolj A; Pahnke A; Wells LA; Masse S; Kim J; Reis L; Momen A; Nunes SS; Wheeler AR; Nanthakumar K; Keller G; Sefton MV; Radisic M Biodegradable scaffold with built-in vasculature for organ-on-a-chip engineering and direct surgical anastomosis. Nat Mater 2016, 15, 669–678. [PubMed: 26950595]

[35]. Fleischer S; Shapira A; Feiner R; Dvir T Modular assembly of thick multifunctional cardiac patches. Proc Natl Acad Sci U S A 2017, 114, 1898–1903. [PubMed: 28167795]

[36]. Cogan SF Neural stimulation and recording electrodes. Annu Rev Biomed Eng 2008, 10, 275–309. [PubMed: 18429704]

[37]. Liu J; Fu TM; Cheng Z; Hong G; Zhou T; Jin L; Duvvuri M; Jiang Z; Kruskal P; Xie C; Suo Z; Fang Y; Lieber CM Syringe-injectable electronics. Nat Nanotechnol 2015, 10, 629–636. [PubMed: 26053995]

[38]. Xie C; Liu J; Fu TM; Dai X; Zhou W; Lieber CM Three-dimensional macroporous nanoelectronic networks as minimally invasive brain probes. Nat Mater 2015, 14, 1286–1292. [PubMed: 26436341]

[39]. Luan L; Wei X; Zhao Z; Siegel JJ; Potnis O; Tuppen CA; Lin S; Kazmi S; Fowler RA; Holloway S; Dunn AK; Chitwood RA; Xie C Ultraflexible nanoelectronic probes form reliable, glial scar-free neural integration. Sci Adv 2017, 3, e1601966. [PubMed: 28246640]

[40]. Chen R; Canales A; Anikeeva P Neural recording and modulation technologies. Nature Reviews Materials 2017, 2, 16093.

[41]. Tee BC; Chortos A; Berndt A; Nguyen AK; Tom A; McGuire A; Lin ZC; Tien K; Bae WG; Wang H; Mei P; Chou HH; Cui B; Deisseroth K; Ng TN; Bao Z A skin-inspired organic digital mechanoreceptor. Science 2015, 350, 313–316. [PubMed: 26472906]

[42]. Kim CK; Adhikari A; Deisseroth K Integration of optogenetics with complementary methodologies in systems neuroscience. Nat Rev Neurosci 2017, 18, 222–235. [PubMed: 28303019]

[43]. Rivnay J; Wang H; Fenno L; Deisseroth K; Malliaras GG Next-generation probes, particles, and proteins for neural interfacing. Sci Adv 2017, 3, e1601649. [PubMed: 28630894]

[44]. Carvalho-de-Souza JL; Treger JS; Dang B; Kent SB; Pepperberg DR; Bezanilla F Photosensitivity of neurons enabled by cell-targeted gold nanoparticles. Neuron 2015, 86, 207–217. [PubMed: 25772189]

[45]. Eom K; Kim J; Choi JM; Kang T; Chang JW; Byun KM; Jun SB; Kim SJ Enhanced infrared neural stimulation using localized surface plasmon resonance of gold nanorods. Small 2014, 10, 3853–3857. [PubMed: 24975778]

[46]. Yoo S; Hong S; Choi Y; Park JH; Nam Y Photothermal inhibition of neural activity with near-infrared-sensitive nanotransducers. ACS Nano 2014, 8, 8040–8049. [PubMed: 25046316]

[47]. Lyu Y; Xie C; Chechetka SA; Miyako E; Pu K Semiconducting Polymer Nanobioconjugates for Targeted Photothermal Activation of Neurons. J Am Chem Soc 2016, 138, 9049–9052. [PubMed: 27404507]

[48]. Jiang Y; Carvalho-de-Souza JL; Wong RC; Luo Z; Isheim D; Zuo X; Nicholls AW; Jung IW; Yue J; Liu DJ; Wang Y; De Andrade V; Xiao X; Navrazhnykh L; Weiss DE; Wu X; Seidman DN; Bezanilla F; Tian B Heterogeneous silicon mesostructures for lipid-supported bioelectric interfaces. Nat Mater 2016, 15, 1023–1030. [PubMed: 27348576]

[49]. Huang H; Delikanli S; Zeng H; Ferkey DM; Pralle A Remote control of ion channels and neurons through magnetic-field heating of nanoparticles. Nat Nanotechnol 2010, 5, 602–606. [PubMed: 20581833]

[50]. Stanley SA; Gagner JE; Damanpour S; Yoshida M; Dordick JS; Friedman JM Radio-wave heating of iron oxide nanoparticles can regulate plasma glucose in mice. Science 2012, 336, 604–608. [PubMed: 22556257]

[51]. Chen R; Romero G; Christiansen MG; Mohr A; Anikeeva P Wireless magnetothermal deep brain stimulation. Science 2015, 347, 1477–1480. [PubMed: 25765068]

[52]. Munshi R; Qadri SM; Zhang Q; Castellanos Rubio I; Del Pino P; Pralle A Magnetothermal genetic deep brain stimulation of motor behaviors in awake, freely moving mice. Elife 2017, 6, e27069. [PubMed: 28826470]

[53]. Rus D; Tolley MT Design, fabrication and control of soft robots. Nature 2015, 521, 467–475. [PubMed: 26017446]

[54]. Feinberg AW; Feigel A; Shevkoplyas SS; Sheehy S; Whitesides GM; Parker KK Muscular thin films for building actuators and powering devices. Science 2007, 317, 1366–1370. [PubMed: 17823347]

[55]. Nawroth JC; Lee H; Feinberg AW; Ripplinger CM; McCain ML; Grosberg A; Dabiri JO; Parker KK A tissue-engineered jellyfish with biomimetic propulsion. Nat Biotechnol 2012, 30, 792–797. [PubMed: 22820316]

[56]. Cvetkovic C; Raman R; Chan V; Williams BJ; Tolish M; Bajaj P; Sakar MS; Asada HH; Saif MT; Bashir R Three-dimensionally printed biological machines powered by skeletal muscle. Proc Natl Acad Sci U S A 2014, 111, 10125–10130. [PubMed: 24982152]

[57]. Raman R; Cvetkovic C; Bashir R A modular approach to the design, fabrication, and characterization of muscle-powered biological machines. Nat Protoc 2017, 12, 519–533. [PubMed: 28182019]

[58]. Cvetkovic C; Rich MH; Raman R; Kong H; Bashir RA 3D-printed platform for modular neuromuscular motor units. Microsystems & Nanoengineering 2017, 3, 17015.

[59]. Shin SR; Shin C; Memic A; Shadmehr S; Miscuglio M; Jung HY; Jung SM; Bae H; Khademhosseini A; Tang XS; Dokmeci MR Aligned carbon nanotube-based flexible gel substrates for engineering bio-hybrid tissue actuators. Adv Funct Mater 2015, 25, 4486–4495. [PubMed: 27134620]

[60]. Raman R; Cvetkovic C; Uzel SG; Platt RJ; Sengupta P; Kamm RD; Bashir R Optogenetic skeletal muscle-powered adaptive biological machines. Proc Natl Acad Sci U S A 2016, 113, 3497–3502. [PubMed: 26976577]

[61]. Park SJ; Gazzola M; Park KS; Park S; Di Santo V; Blevins EL; Lind JU; Campbell PH; Dauth S; Capulli AK; Pasqualini FS; Ahn S; Cho A; Yuan H; Maoz BM; Vijaykumar R; Choi JW; Deisseroth K; Lauder GV; Mahadevan L; Parker KK Phototactic guidance of a tissue-engineered soft-robotic ray. Science 2016, 353, 158–162. [PubMed: 27387948]

[62]. Phan L; Kautz R; Leung EM; Naughton KL; Van Dyke Y; Gorodetsky AA Dynamic Materials Inspired by Cephalopods. Chemistry of Materials 2016, 28, 6804–6816.

[63]. Pikul JH; Li S; Bai H; Hanlon RT; Cohen I; Shepherd RF Stretchable surfaces with programmable 3D texture morphing for synthetic camouflaging skins. Science 2017, 358, 210–214. [PubMed: 29026040]

[64]. Yu C; Li Y; Zhang X; Huang X; Malyarchuk V; Wang S; Shi Y; Gao L; Su Y; Zhang Y; Xu H; Hanlon RT; Huang Y; Rogers JA Adaptive optoelectronic camouflage systems with designs inspired by cephalopod skins. Proc Natl Acad Sci U S A 2014, 111, 12998–13003. [PubMed: 25136094]

[65]. Li J; Celiz AD; Yang J; Yang Q; Wamala I; Whyte W; Seo BR; Vasilyev NV; Vlassak JJ; Suo Z; Mooney DJ Tough adhesives for diverse wet surfaces. Science 2017, 357, 378–381. [PubMed: 28751604]

[66]. Zhao Q; Lee DW; Ahn BK; Seo S; Kaufman Y; Israelachvili JN; Waite JH Underwater contact adhesion and microarchitecture in polyelectrolyte complexes actuated by solvent exchange. Nat Mater 2016, 15, 407–412. [PubMed: 26779881]

[67]. Gebbie MA; Wei W; Schrader AM; Cristiani TR; Dobbs HA; Idso M; Chmelka BF; Waite JH; Israelachvili JN Tuning underwater adhesion with cation-pi interactions. Nat Chem 2017, 9, 473–479. [PubMed: 28430190]

[68]. Iturri J; Xue L; Kappl M; García-Fernández L; Barnes WJP; Butt H-J; del Campo A Torrent Frog-Inspired Adhesives: Attachment to Flooded Surfaces. Advanced Functional Materials 2015, 25, 1499–1505.

[69]. Drotlef D-M; Stepien L; Kappl M; Barnes WJP; Butt H-J; del Campo A Insights into the Adhesive Mechanisms of Tree Frogs using Artificial Mimics. Advanced Functional Materials 2013, 23, 1137–1146.

[70]. Xue L; Sanz B; Luo A; Turner KT; Wang X; Tan D; Zhang R; Du H; Steinhart M; Mijangos C; Guttmann M; Kappl M; Del Campo A Hybrid Surface Patterns Mimicking the Design of the Adhesive Toe Pad of Tree Frog. ACS Nano 2017, 11, 9711–9719. [PubMed: 28885831]

[71]. Lee H; Lee BP; Messersmith PB A reversible wet/dry adhesive inspired by mussels and geckos. Nature 2007, 448, 338–341. [PubMed: 17637666]

[72]. Mahdavi A; Ferreira L; Sundback C; Nichol JW; Chan EP; Carter DJ; Bettinger CJ; Patanavanich S; Chignozha L; Ben-Joseph E; Galakatos A; Pryor H; Pomerantseva I; Masiakos PT; Faquin W; Zumbuehl A; Hong S; Borenstein J; Vacanti J; Langer R; Karp JM A biodegradable and biocompatible gecko-inspired tissue adhesive. Proc Natl Acad Sci U S A 2008, 105, 2307–2312. [PubMed: 18287082]

[73]. Frost SJ; Mawad D; Higgins MJ; Ruprai H; Kuchel R; Tilley RD; Myers S; Hook JM; Lauto A Gecko-inspired chitosan adhesive for tissue repair. NPG Asia Materials 2016, 8, e280.

[74]. Luo Z; Jiang Y; Myers BD; Isheim D; Wu J; Zimmerman JF; Wang Z; Li Q; Wang Y; Chen X; Dravid VP; Seidman DN; Tian B Atomic gold-enabled three-dimensional lithography for silicon mesostructures. Science 2015, 348, 1451–1455. [PubMed: 26113718]

[75]. Cho WK; Ankrum JA; Guo D; Chester SA; Yang SY; Kashyap A; Campbell GA; Wood RJ; Rijal RK; Karnik R; Langer R; Karp JM Microstructured barbs on the North American porcupine quill enable easy tissue penetration and difficult removal. Proc Natl Acad Sci U S A 2012, 109, 21289–21294. [PubMed: 23236138]

[76]. Yang SY; O'Cearbhaill ED; Sisk GC; Park KM; Cho WK; Villiger M; Bouma BE; Pomahac B; Karp JM A bio-inspired swellable microneedle adhesive for mechanical interlocking with tissue. Nat Commun 2013, 4, 1702. [PubMed: 23591869]

[77]. Yi J; Wang Y; Jiang Y; Jung IW; Liu W; De Andrade V; Xu R; Parameswaran R; Peters IR; Divan R; Xiao X; Sun T; Lee Y; Park WI; Tian B 3D calcite heterostructures for dynamic and deformable mineralized matrices. Nat Commun 2017, 8, 509. [PubMed: 28894143]

[78]. Chen YC; Yang H Octopus-Inspired Assembly of Nanosucker Arrays for Dry/Wet Adhesion. ACS Nano 2017, 11, 5332–5338. [PubMed: 28448714]

[79]. Lee H; Um DS; Lee Y; Lim S; Kim HJ; Ko H Octopus-Inspired Smart Adhesive Pads for Transfer Printing of Semiconducting Nanomembranes. Adv Mater 2016, 28, 7457–7465. [PubMed: 27322886]

[80]. Baik S; Kim DW; Park Y; Lee TJ; Ho Bhang S; Pang C A wet-tolerant adhesive patch inspired by protuberances in suction cups of octopi. Nature 2017, 546, 396–400. [PubMed: 28617467]

[81]. Pan F; Gao S; Chen C; Song C; Zeng F Recent progress in resistive random access memories: Materials, switching mechanisms, and performance. Materials Science & Engineering R-Reports 2014, 83, 1–59.

[82]. Sheridan PM; Cai F; Du C; Ma W; Zhang Z; Lu WD Sparse coding with memristor networks. Nat Nanotechnol 2017, 12, 784–789. [PubMed: 28530717]

[83]. van de Burgt Y; Lubberman E; Fuller EJ; Keene ST; Faria GC; Agarwal S; Marinella MJ; Alec Talin A; Salleo A A non-volatile organic electrochemical device as a low-voltage artificial synapse for neuromorphic computing. Nat Mater 2017, 16, 414–418. [PubMed: 28218920]

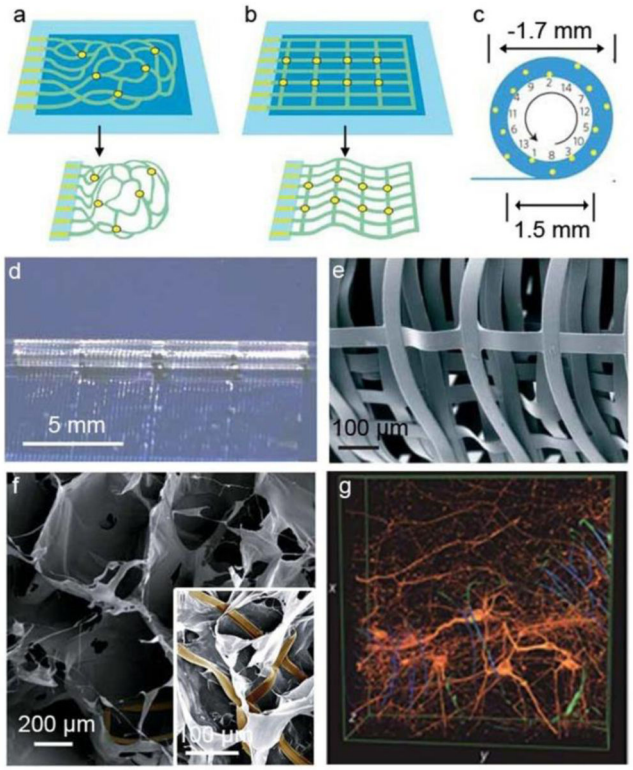

Figure 1. Macroporous electronics-innervated synthetic tissues.

Device fabrication schematics of **a**, Reticular nanowire FET devices and **b**, Mesh-like nanowire FET devices. Light blue: silicon oxide substrates; blue: nickel sacrificial layers; green: nanoelectronic scaffolds; yellow dots: individual nanowire FETs. **c**, 14 nanowire FETs evenly distributed throughout a fully rolled-up mesh device. Upper panel, schematic diagram of the nanowire FET position (yellow dots). **d**, Photograph of a partially rolled-up mesh device. **e**, SEM image of a loosely packed mesh nanoelectronic scaffolds, showing the macroporous structure. **f**, SEM images of a mesh nanoelectronic/alginate scaffold. The inset highlights the epoxy ribbons (false-coloured in brown) used to support and passivate FET interconnects. **g**, 3D reconstructed confocal images of rat hippocampal neurons after a two-week culture in Matrigel on reticular nanoelectronic scaffolds. Red (Alexa Fluor 546): neuronal β-tubulin; yellow (rhodamine 6G): epoxy ribbons. The metal interconnects (false-colored in blue) are imaged in reflected light mode. Dimensions x: 317 μm; y: 317 μm; z: 100 μm. Figures are reproduced with permission from ref 21. Copyright 2012 Nature Publishing Group.

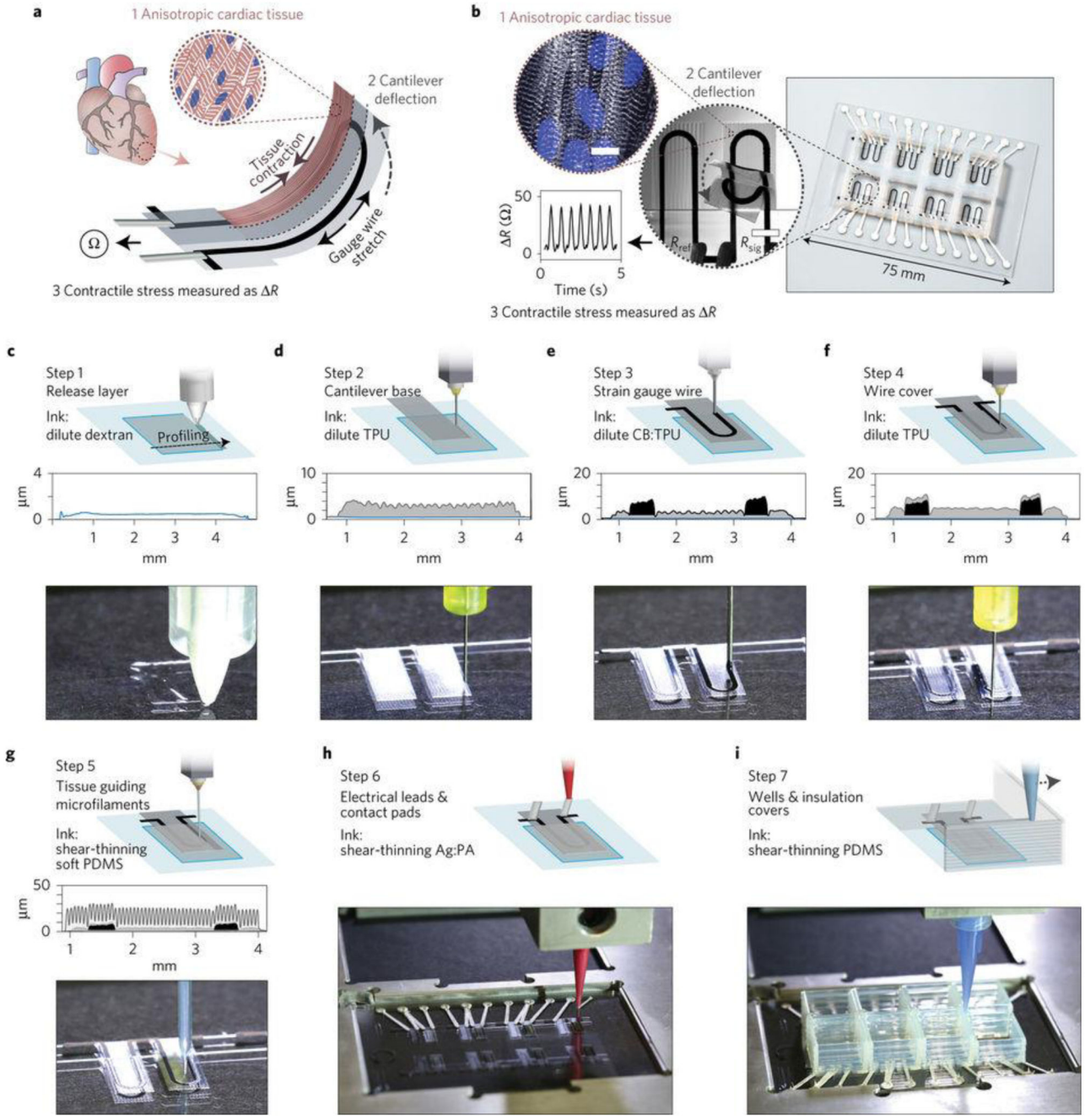

Figure 2. Printed cell-integrated electronics.

a, Device working principle. When an anisotropic engineered cardiac tissue contracts, it will deflect a cantilever substrate and stretch a soft strain sensor embedded in the cantilever. The contractile stress of the tissue can then yield resistance change in the sensor. **b**, Images showing a fully printed final device. Inset 1: Confocal microscopy image of immunostained cardiac tissue on the cantilever surface. Blue, DAPI nuclei stain. White, α-actinin. Inset 2: An image of a cantilever deflecting upon tissue contraction. Inset 3: Representative resistance signal from the embedded strain sensor. **c–i**, Schematic diagrams and photos

showing the automated printing of the device on a glass slide substrate in seven sequential steps. A stylus profiling cross-sectional contour of the cantilever is also shown for steps 1–5. For details of the printing, please refer to ref 30. Figures are reproduced with permission from ref 30. Copyright 2017 Nature Publishing Group.

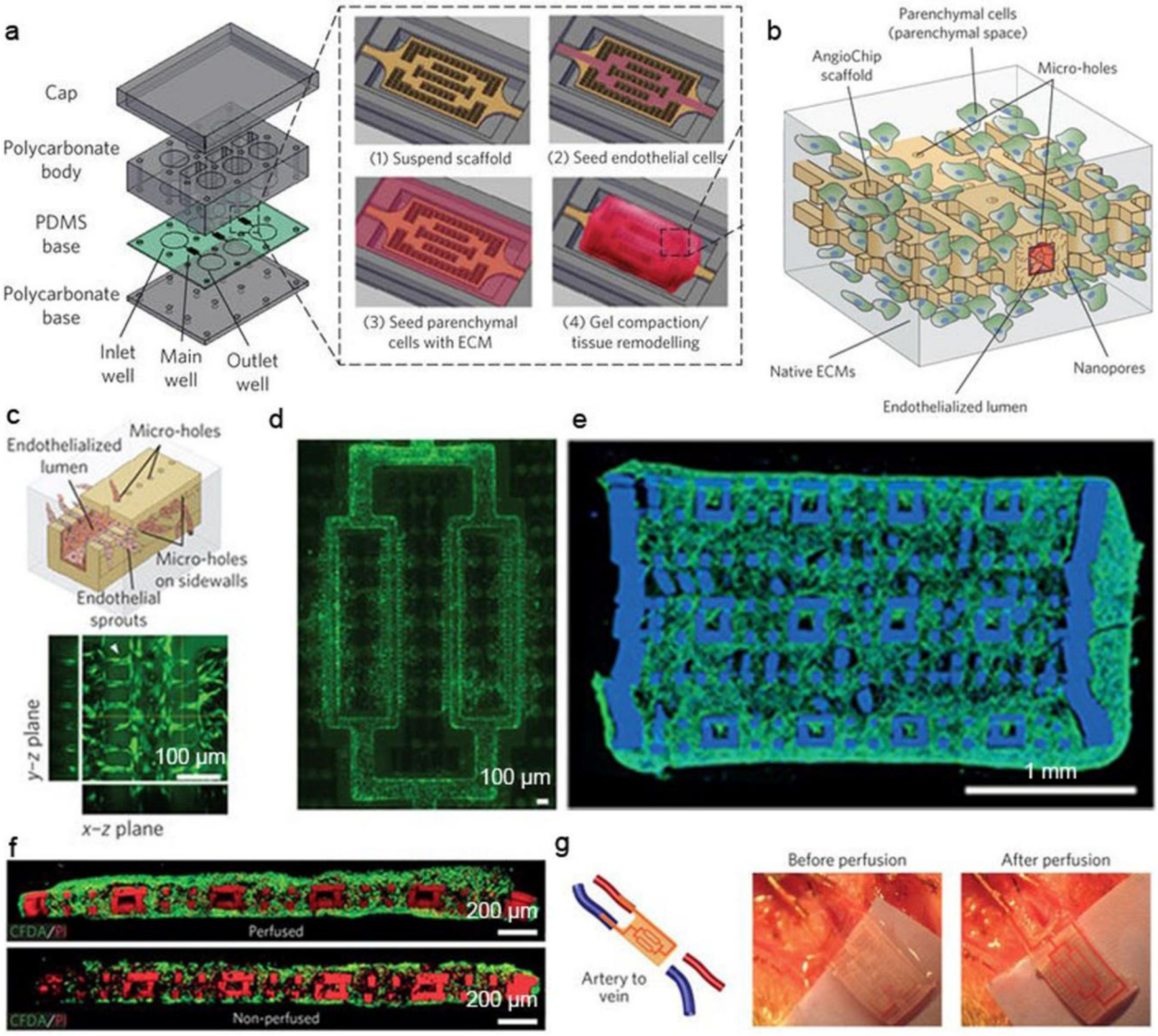

Figure 3. Microfluidics-enabled tissue constructs.

a, Schematic diagrams of the bioreactor assembly and the vascularized tissue construction. **b**, Schematic of an area outlined by dashed box in insert of **a(4)**. **c**, Schematic of endothelial cells migrating and sprouting from the inner lumen of the microchannel to the surrounding parenchyma through the built-in 20 μm micro-holes on the sidewalls. **d**, Fluorescent image of endothelial cells (green) sprouting from the channel networks into the parenchymal space on day 2 (n=4). **e**, Immunostaining of F-actin (green) of the cross-section of an endothelialized thick multi-layer human cardiac tissue with 20 μm micro-holes on day 3 based on fibrin gel and human embryonic stem cells derived cardiac monocytes (n=3). **f**, CFDA (green)- and PI (red)-stained images of the cross-section of rat cardiac tissues with 10 μm micro-holes cultivated with or without medium perfusion on day 7 (n=3). Scaffold also stains red. **g**, Surgical anastomosis of the cardiac tissue on the rat femoral vessels in the artery-to-vein graft. Blood perfusion was established immediately after anastomosis. Papers

were placed under the implants during imaging for better visual contrast. Figures are reproduced with permission from ref 34. Copyright 2016 Nature Publishing Group.

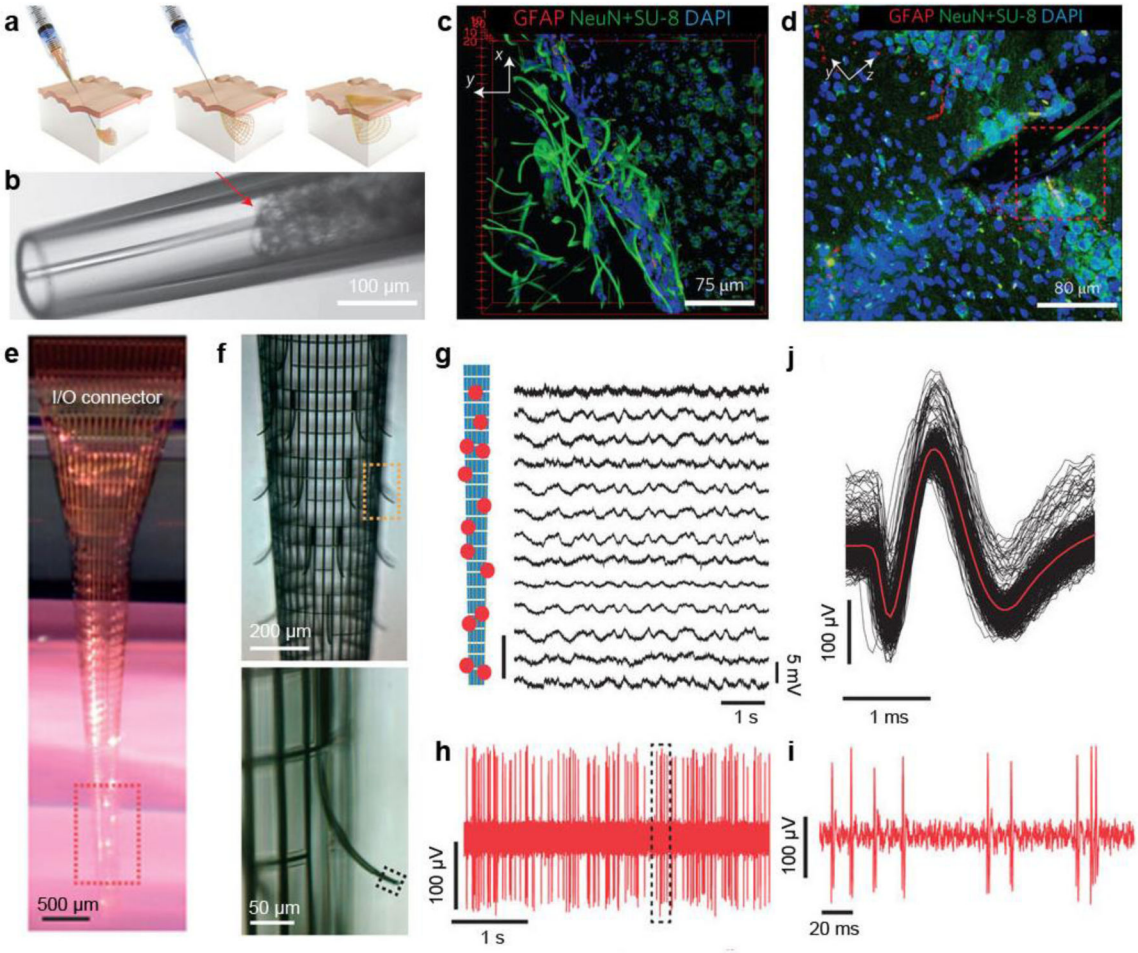

Figure 4. Minimally-invasive brain probes.

a, Schematics of injectable electronics. Red-orange lines highlight the overall mesh structure and indicate the regions of supporting and passivating polymer mesh layers. **b**, Images of mesh electronics injection through a glass needle (Inner diameter = 95 μm) into ×1 PBS solution: bright-field microscopy image of the mesh electronics immediately before injection into solution. **c**, 3D reconstructed confocal image at the interface between the mesh electronics and subventricular zone. **d**, Projection of the 3D reconstructed confocal image from a 30-μm thick, 317-μm-long and 317-μm-wide volume from a coronal slice of the hippocampal region five weeks post-injection of the mesh electronics. **e**, Photograph of a typical macroporous nanoelectronic brain probe suspended in buffer with a cylindrical shape. Its back end is attached to the carrier substrate (the dark piece in the back) at the top of the image. **f**, (Top) micrograph of the sensor area of the probe outlined by the red dashed box in (e); (Bottom) Zoomed-in view of the outward bent supporting arm and sensor outlined by the yellow dashed box in (f). **g**, Acute multiplexed local field potentials recording from 13 nanowire FET sensors following probe insertion into the somatosensory cortex. Relative positions of the 13 sensors are marked in the schematic on the left. **h**, Representative acute single-unit recording from Pt electrode sensors. **i**, Zoomed-in view of nine single-unit events outlined in (f). **j**, Superimposed 94 single-unit events from the

recording in (h). Figure a-d are reproduced with permission from ref 37. Copyright 2015 Nature Publishing Group. Figure e-j are reproduced with permission from ref 38. Copyright 2015 Nature Publishing Group.

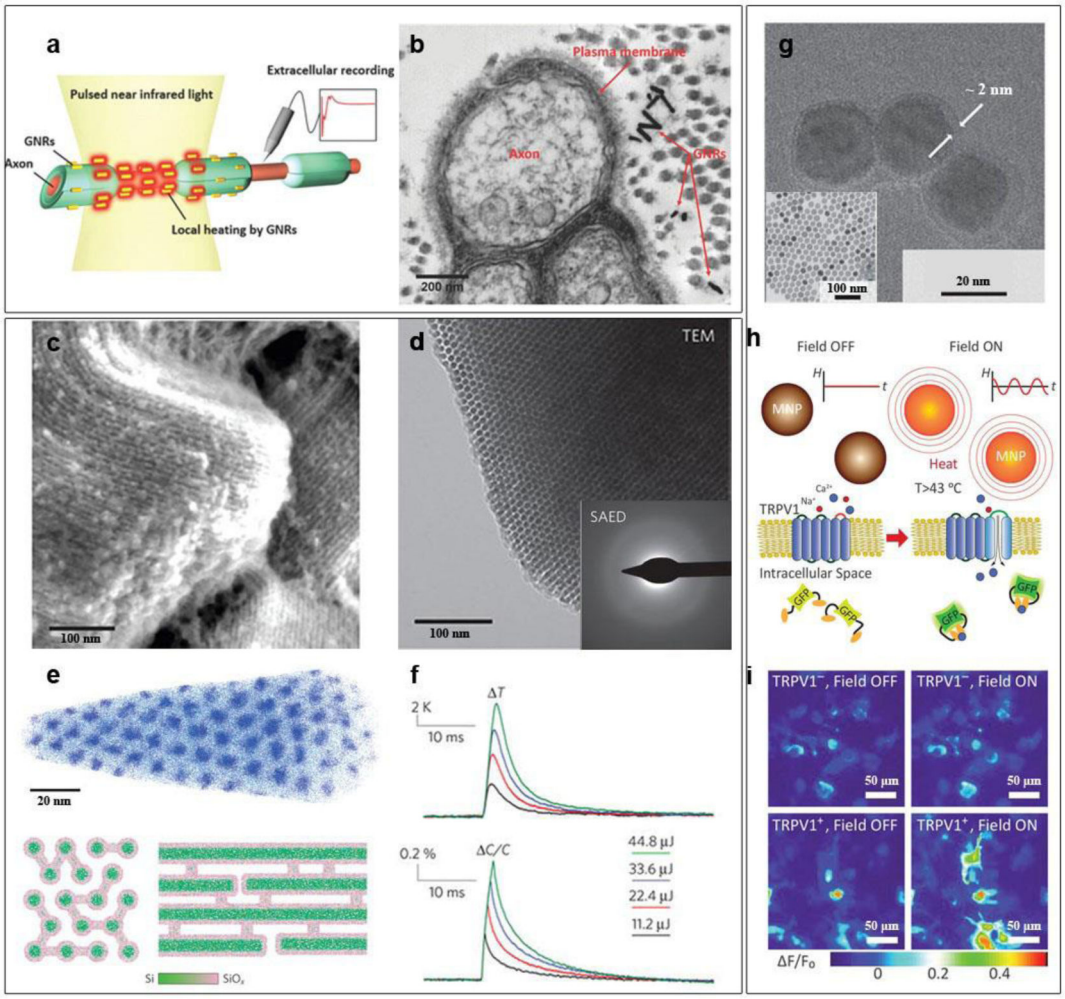

Figure 5. Remote neural modulation.

a, Gold nanorods distributed in the vicinity of the plasma membrane of nerve tissues are designed to absorb a light energy at 980 nm wavelength. **b**, TEM image showing a cross-sectional view of rat sciatic nerve after injecting gold nanorods. **c**, SEM image reveals periodic arrangement of Si nanowire assembly. **d**, TEM image of silicon mesostructures and SAED pattern (inset) showing an amorphous atomic structure. **e**, (Upper) Atom-probe tomography of one as-deposited sample (without SiO_2 removal) exhibits hexagonal packing of Si nanowires in SiO2 matrix. For clarity, only 5% of total Si (blue dots) and O (cyan dots) are displayed. End- (bottom left) and side-view (bottom-right) schematics of mesostructured Si illustrate the graded Si/SiO_x (green/pink) interfaces and the observed chemical heterogeneity between nanowires and micro-bridges. **f**, Averaged local solution temperature (top) and bilayer capacitance (bottom) dynamics following laser pulses with different input energies. **g**, TEM image of Fe_3O_4 nanoparticles with a 2-nm PEG shell after surface modification, (inset) the as-synthesized Fe_3O_4 nanoparticles. **h**, Experimental scheme. Magnetic field stimulation ("Field ON") of TRPV1 from Fe_3O_4 nanoparticles heating is visualized by gCaMP6s fluorescence changes. **i**, Color maps of fluorescence intensity changes for $TRPV1^-$ and $TRPV1^+$ HEK293FT cells before and during magnetic field

stimulus. Figure a-b are reproduced with permission from ref 45. Copyright 2014 Wiley-VCH. Figure c-f are reproduced with permission from ref 48. Copyright 2016 Nature Publishing Group. Figure g-i are reproduced from ref 51. Copyright 2015 AAAS.

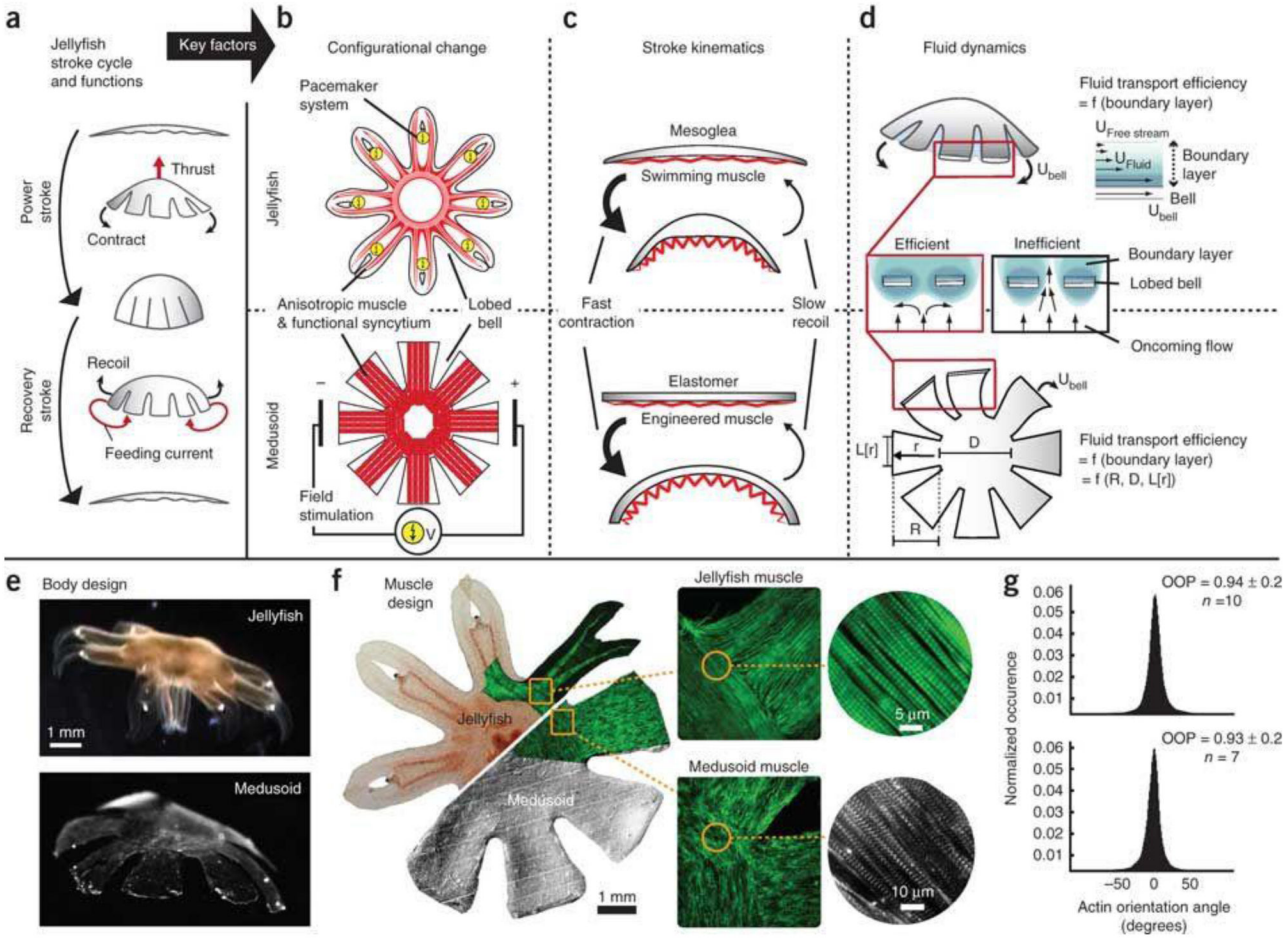

Figure 6. Artificial jellyfish.

a, Schematic diagram of jellyfish stroke cycle generating thrust during the power stroke, and feeding currents during the recovery stroke. **b**, Schematics showing the configurational change. **c**, Diagrams showing the stroke kinematics. In the bilayered design of jellyfish (top) and medusoid (bottom), a flexible elastomer opposes an actuator, which promotes asymmetric stroke patterns: active, fast contraction and passive, slow recoil. **d**, Illustration of the fluid dynamics. **e**, Design of jellyfish (top) and free-swimming medusoid construct (bottom). **f**, The 2D muscle architecture of a jellyfish (top) was reverse-engineered in medusoids (bottom). Left: Composite brightfield image overlaid with F-actin stain (green) of muscle cell monolayer. Square inset: Close-up on muscle organization at lobe-body junction; F-actin stain (green). Insets show the microstructure of single myofibril layer; F-actin stain (green), sarcomeric α-actinin (gray). **g**, Distribution of actin fiber orientation angles within single myofibril layer. Statistical analysis of multiple fields of view revealed no significant difference in the orientation organization parameter (OOP) ($P = 0.61$, $n = 10$; two-sample t-test). Figures are reproduced with permission from ref 55. Copyright 2012 Nature Publishing Group.

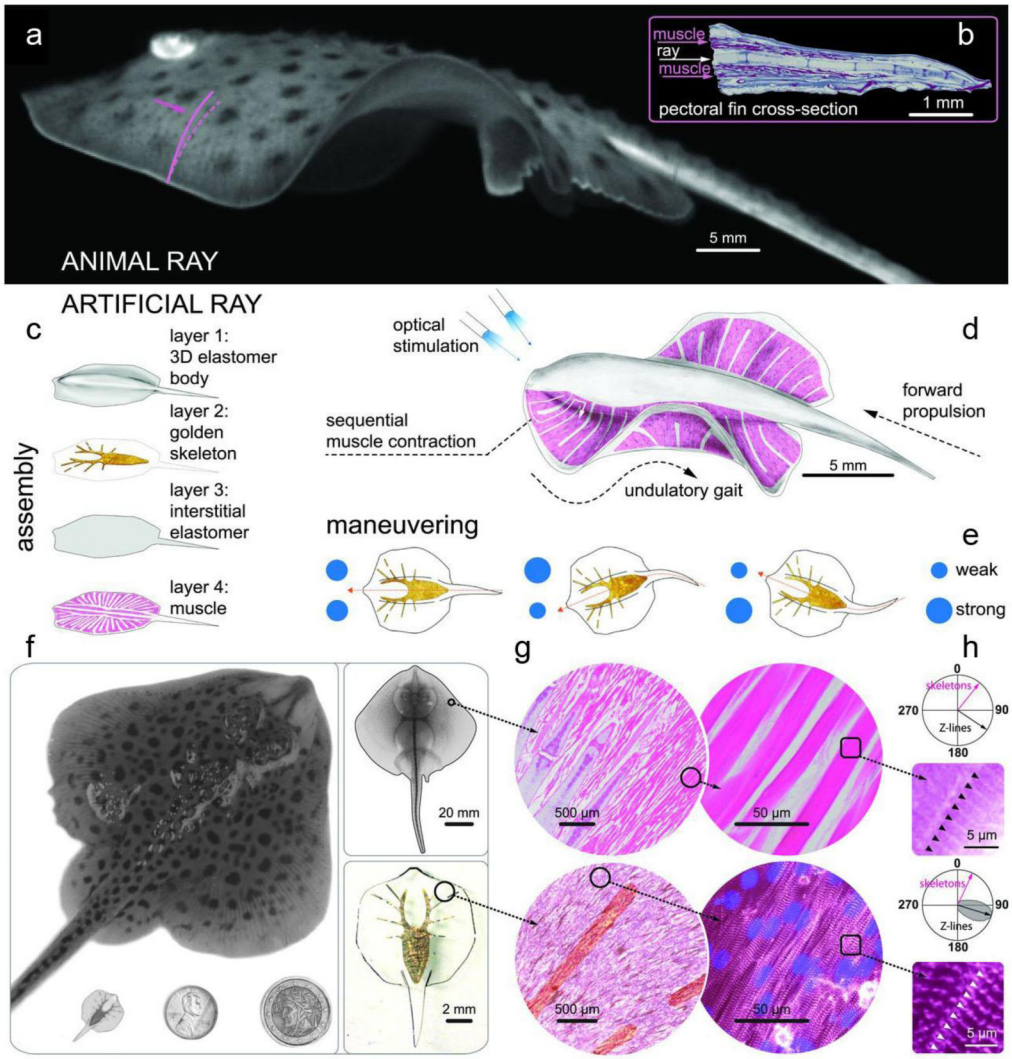

Figure 7. An artificial sting ray.

a, A live Little skate, *Leucoraja erinacea*, swimming and **b**, its musculoskeletal structure. **c**~**e**, Tissue-engineered ray with, **c**, four body layers, **d**, basic design, and **e**, the principle of phototactic control. Upon optical stimulation, the engineered ray induces sequential muscle contraction via serpentine-patterned muscle tissues, generates undulatory locomotion, and sustains steady forward swimming. **f**, Comparison between a skate (top) and a tissue-engineered ray (bottom left). One penny and a two Euros coin (bottom middle and right) are shown for size comparison. **g** and **h**, Musculoskeletal meso (**g**) and micro (**h**)-architecture of a skate, *L. erinacea* (top), is recapitulated in a tissue engineered ray (bottom). For more details of the panel, please refer to Ref 61. **h**, Orientation of the Z-lines. In skate, the lines are indicated with black arrow and black triangles. In tissue engineered ray, the lines are shown with black arrow with gray distribution and white triangles. In both cases, Z-lines are perpendicular to the skeleton rays (pink arrows). Figures are reproduced from ref 61.

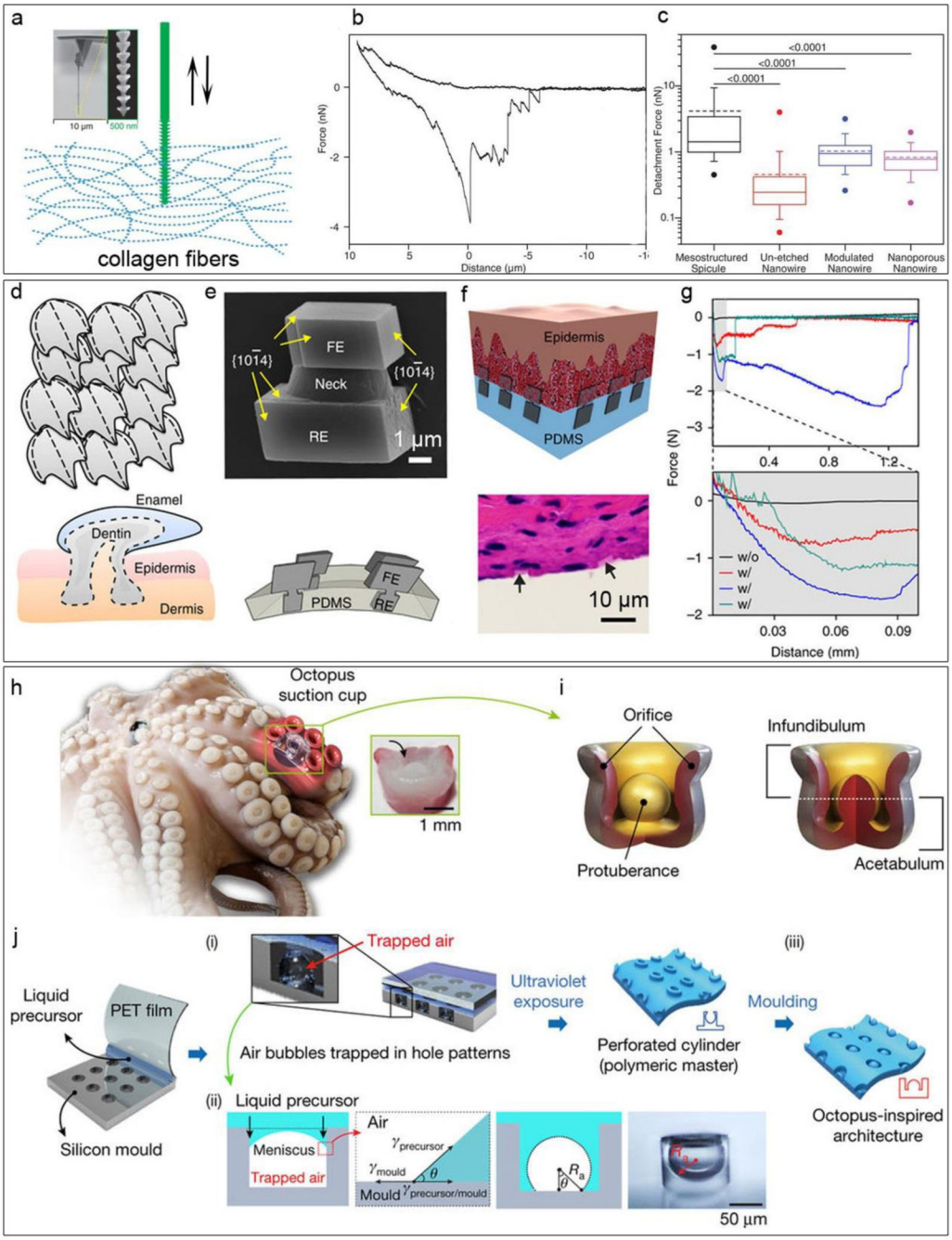

Figure 8. Underwater adhesion.

a, Schematic diagram of the interaction between skeleton-like anisotropic Si spicules and collagen fiber networks. Insets displace the spicule-based AFM probe at different magnifications. **b**, Representative force-distance curves collected using an individual Si spicule as a probe. **c**, Box-and-whisker plots of forces required to detach skeleton-like anisotropic silicon spicules (black), un-etched Si nanowires (red), diameter-modulated Si nanowires (blue), and nanoporous Si nanowires (purple). Half of the data points are within the box, and 80% are within the whiskers. Solid and dashed lines mark the median and

mean, respectively. The dots represent maximum and minimum values. The means of detachment force are 4.16 nN (skeleton-like anisotropic silicon spicules), 0.455 nN (un-etched nanowire), 1.03 nN (modulated nanowire), and 0.827 nN (nanoporous nanowire). n = 50 force-distance curves per probe, and numbers above bars indicate the P value of the Mann-Whitney test. **d**, Schematic diagram of placoid scales, showing heterojunctions and compartments. **e**, (Top) SEM image of a calcite heterostructure grown by a tectonic approach, showing an rooted end (RE), a neck and an functional end (FE). (bottom) Schematic representation of the final mineral matrix. **f** and **g**, Flexible tissue adhesives with inorganic localized adhesions, demonstrated with a schematic **f** (top), H&E staining image **f** (bottom) and force-distance recordings **g**. **h**, *O. vulgaris tentacles*. Inset, a transverse-section image showing the anatomical architecture. **i**, Illustrations of the sucker structure. **j**, Fabrication schema of the octopus-inspired adhesive. See ref 80 for details. Panels **a-c** are reproduced from ref 74. Copyright 2015 AAAS. Panels **d-g** are reproduced from ref 77. Copyright 2017 Nature Publishing Group. Panels **h-j** are reproduced from ref 80. Copyright 2017 Nature Publishing Group.